ELECTRICAL PROPERTIES OF ANNEALED TRANSPARENT AMORPHOUS INDIUM ZINC OXIDE THIN FILMS

By

Andrew Noble Cavendor

ProQuest LLC.
789 East Eisenhower Parkway
P.O. Box 1346
Ann Arbor, MI 48106 – 1346

A thesis submitted to the Faculty and the Board of Trustees of the Colorado School of Mines in partial fulfillment of the requirements for the degree of Master of Science (Materials Science).

Golden, Colorado

Date 11/8/07

Signed: Andrew N. Cavendor
Andrew N. Cavendor

Signed: Ryan O'Hay
Dr. Ryan P. O'Hayre
Thesis Advisor

Signed:
Dr. David S. Ginley
Thesis Co-Advisor

Golden, Colorado
Date 11-8-07

Signed: J J Moore
Dr. John J. Moore
Professor and Program Director
Materials Science

ABSTRACT

Transparent conducting oxides (TCOs) are a class of materials that provide tunable electrical properties while maintaining high optical transparency. There many applications for amorphous indium zinc oxide (α-IZO), an important amorphous TCO, but one of its potential applications is in transparent thin film transistors (TTFTs). α-IZO's electrical properties are easily manipulated making it suitable for TTFT applications. However, DC magnetron-sputtered resistive thin films of α-IZO exhibit a low temperature ($100 < T < 200$ °C) time dependent thermally activated increase in conductivity. Such a change in conductivity would render TTFTs unusable as an electronic switch. This thesis explores the approximately seven orders of magnitude transformation seen in α-IZO, from a resistive to conductive thin film. Amorphous 84/16 at. % IZO was characterized by optical reflection and transmission spectra, four-point probe measurements, and x-ray diffraction spectra. α-IZO samples were transparent in the visible spectrum before and after annealing at temperatures ranging from 120-170 °C. X-ray diffraction detected a small increase in ordering of some annealed films. A one dimensional diffusion model and a nucleation and growth Avrami-Johnson-Mehl model were employed to explain the mechanism behind the approximately seven orders of magnitude increase in conductivity. The results indicate that the thermal increase in electrical conductivity cannot be explained by oxygen diffusion. Instead, the transformation might be driven by a three dimensional nucleation and growth process.

TABLE OF CONTENTS

LIST OF FIGURES

LIST OF TABLES

ACKNOWLEDGEMENTS

I would like to express my sincerest gratitude to David Ginley, my scientific advisor, for providing me with such a wonderful environment to learn and to grow at the National Renewable Energy Laboratory. The scientific staff was a pleasure to work with, and helped me whenever there was need. Special thanks go to John Perkins who mentored and provided me unending help in building my measurement system and in the analysis of the results. My gratitude goes out to Dane Gillaspe, Chris Gorrie, Joe Berry, Anna Duda, and Phil Parilla for all helping me with the details of my research, as well as Matthew Dabney and Miakel van Hest who were always there to support me and help me through the process, and became dear friends. I want to thank my advisor from the Colorado School of Mines, Ryan O'Hayre, for all the work, support, and guidance he provided. Lastly, to all my friends and family, who's never ending love and support helped to inspire and motivate me throughout.

CHAPTER 1 – INTRODUCTION

1.1 Research Motivations and Objectives

Transparent conducting oxides (TCOs) are a class of oxide materials that can be tuned to provide high electrical conductivity commensurate with high optical transparency. TCOs have many important uses in the optoelectronic industries, including applications in solar cells, electro-chromic windows, and flat-panel displays. Indium zinc oxide (IZO) is an important new amorphous TCO with large-scale applications in displays and potential applications in transparent thin film transistors (TTFTs). α-IZO, when optimized, is a transparent n-type semiconductor with > 80 percent optical transmittance in the visible spectrum [1]. α-IZO is amorphous between ~54-85 atomic percent In/Zn [2] and when optimized has conductivities > 10^3 Scm^{-1} [2-4] with mobilities exceeding >50 $cm^2V^{-1}s^{-1}$ [4] and carrier concentrations > 10^{20} cm^{-3} [5], all of which depend on the deposition conditions. The large composition range of α-IZO allows process flexibility as well as the potential to reduce materials costs by using less indium. In this region of the phase diagram, sputtered thin films are stable, uniform, and surface roughness is ~0.2 nm [6, 7]. α-IZO can be deposited at room temperature, lowering the economic cost. Low temperature deposition also allows film deployment on a number of low-T, flexible substrates (such as plastics), thereby improving the range of application.

In addition to photovoltaic and display applications there is an emerging collection of applications for TTFTs. Figure 1.1 illustrates the use of IZO in a TTFT application. Transistors require a material that can be deposited as either resistive or conductive films while maintaining high transparency, high mobility, a smooth surface, thermal stability, and chemical stability for etching [8]. By adding oxygen during film deposition, highly resistive films 10^{-6} S/cm [4] can be produced, thereby granting the capacity to make TTFTs with both conductive source/drain contacts and resistive active layer [8-10], as seen in Figure 1.1.

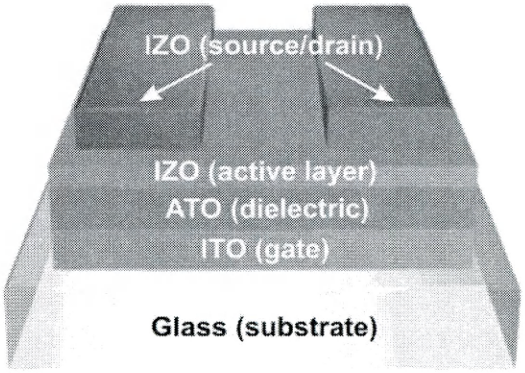

Figure 1.1 – Schematic illustration of the IZO-based bottom-gate TFT structure [8].

Recent observations indicate that resistive IZO suffers from instabilities, which may render it unusable in TTFT applications. In particular, IZO manifests persistent photoconductivity upon exposure to ultraviolet light [11]. The resulting effect in transistors can been seen in Figure 1.2, which shows the on and off characteristics of an IZO TTFT once exposed to ultraviolet light. The ultraviolet light switches the IZO TTFT to a permanent 'on' state where current continually flows and renders the TTFT unusable Figure 1.2 (b). Also, resistive α-IZO exhibits a rapid and dramatic permanent increase in conductivity upon exposure to intermediate (100-200°C) temperatures. This thermal effect has potentially huge consequences for all α-IZO applications. While both instabilities present significant concern, in the present study, this investigation is restricted to the thermal instability problem in IZO. This thermal instability quandary results in a permanent, orders of magnitude increase in conductivity when originally resistive IZO is exposed to intermediate temperatures in the range of 100-200 °C. As will be seen, our exploration of this effect necessitates a fundamental inquiry into the electronic nature of amorphous IZO and the source of the instabilities.

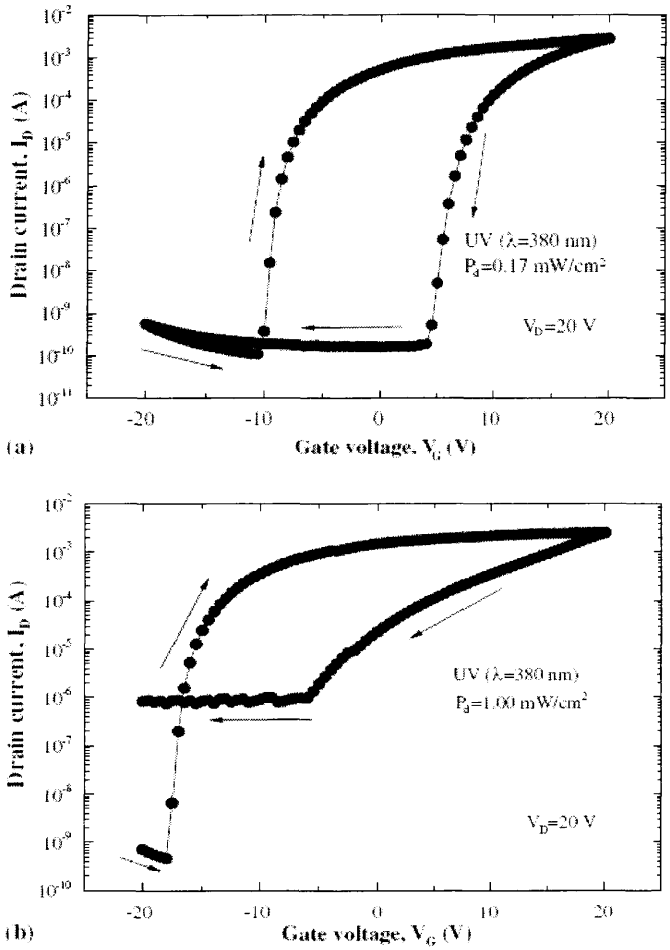

Figure 1.2 – Transfer characteristics for a IZO TTFT measured in double sweep, irradiated with a monochromatic light of 380 nm (UV), with optical power density of 0.17 mW/cm^2 (a) and 1.00 mW/cm^2 (b) [11].

1.2 Applications and Outlook of TCOs

Simultaneous high transparency in the visible spectrum and useful conductivities make TCOs an important class of technological materials. Energy efficient windows are among the most highly mass produced commercial items incorporating TCO technology today [12, 13]. Glass can be coated with a TCO to give it the ability to reflect thermal infrared heat. This ability is possible because TCO materials exhibit low emissivities in the infrared spectrum, and also absorb harmful ultraviolet light [13]. Houses are able to regulate temperature with lower costs using these infrared efficient architectural windows. By area, the most deposited TCO today is SnO_2 [14],which is used in these window applications.

Research on transparent conducting oxides has intensified in the last few years due to growing applications in display technologies and photovoltaics. Cathode Ray Tube (CRT) monitors are very bulky; however, by exploiting TCOs as the front-surface electrode on a monitor, flat panel displays (FPD) have replaced CRT monitors with less space and weight. Electrical signals are sent to the light emitting devices in a FPD though a matrix of TCOs. Since the TCO is transparent to the emitted light, visual information can pass through the TCO unimpeded to the eyes of onlookers. Similarly, solar cells use TCOs as the front surface electrode; however, light is let into the device instead of out, as in a FPD. Photovoltaics (PV) need a conducting layer to collect charge carriers while letting the light pass through to the absorber layer, where the carriers are effectively created [15]. In the past, silver was used to collect the carriers, but silver is not transparent and reduces the efficiency of photovoltaic cell by covering crucial solar collecting areas. As devices using TCOs, displays and PV, become larger the demands on optoelectronic properties, as well as processing properties, increase as well.

There are a variety of other applications for TCOs. Automatically dimming rear-view mirrors in automobiles, and electrically controlled 'smart' windows incorporate an electrochromic film with TCOs to filter light to pleasant levels. TCOs are used in cars and grocer freezers by to keep windows frost-free when a current is applied. In xerographic machines, TCOs are used to dissipate static electricity. Touch sensitive TCOs can be incorporated with display technologies for touch-control panels. TCOs can

also be constructed into transparent electro-magnetic shields, invisible security circuits on windows, and transparent radio antennas built into automobile windows [12]. Even many electronic gadgets, such as cell phones and mp3 players, are completely dependent on TCOs in their displays.

Transistors are important because of their use in the semiconductor industry as a computational device in computers. By making transistors transparent, a whole new aspect to the industry can be developed allowing transistors to be incorporated into glasses, such as windows in cars. Current research has been directed towards transparent thin film transistors or TTFTs [8-11, 16]. Current thin film transistors (TFTs), as used in liquid crystal displays (LCDs) for example, use amorphous silicon (α-Si) as the active channel layer, which has low mobility (< 1 $cm^2V^{-1}s^{-1}$) [16] limiting refresh rates. Also, α-Si has light induced degradation and must be masked, lowering light output of the LCD. In the last couple of years researchers have begun to think about oxide based transistors as both improving performance and being transparent. IZO is one of the most exciting candidates for this as it potentially has high mobilities, and is transparent, providing a path toward transparent thin film transistors (TTFTs). A transistor is an electronic switch operated by applying a voltage across contacts allowing current to flow. The applications for TCOs are ever increasing.

1.3 Transparent Conducting Oxides

The first account of a TCO was in 1907 by Badeker [17], who used a glow discharge chamber to deposit thin films of Cd and discovered that oxidizing the films made them transparent while retaining their electrical conductivity. Since then, many new TCOs have been found and utilized in commercial applications. Such films are characterized by their transparency due to a high band gap, as many oxides are; however, only a few are electrically conductive such as SnO_2, In_2O_3, ZnO, Ga_2O_3, and CdO [18, 19]. Most well known TCOs are n-type conductors, meaning that electrons are the most prevalent conducting species. "Electron-hole", or p-type conductors, are not widely used because oxygen bonds easily trap holes lowering their mobility [20]. Electrical properties of n-type TCOs come from two different sources: doping and oxygen vacancies. For

instance, In_2O_3 can be doped with various elements such as fluorine, tin, molybdenum, and titanium which substitute an aliovalent ion for the In^{3+} changing the electronic structure by freeing carriers [18, 21, 22]. The carrier concentration may be manipulated by up to nine orders of magnitude by changing the number of oxygen vacancies in both tin doped indium oxide (ITO) and zinc doped indium (IZO) [4, 18]. ITO is used as the standard TCO in electronic applications because of its excellent conductivity (10^4 S/cm). ITO is deposited at elevated temperatures (200-500 °C) to produce this high conductivity making it expensive to deposit as well as unsuitable for some flexible polymer-based substrates [12]. With the ever-increasing price of indium, ITO has become expensive because it uses a high content of indium (90 atomic percent). TCOs with reduced indium content and lower deposition temperatures are extremely desirable.

This study concentrates on the TCO amorphous indium zinc oxide (α-IZO). IZO has increasingly become commercially important and the favored standard composition is 84 atomic percent In/Zn, to obtain the largest possible conductivity, typically ~3000 S/cm [2]. Previous work by Leenheer [4], seen in Figure 1.3, demonstrates this high conductivity may be reduced 9 orders of magnitude by introducing oxygen during deposition. Thin films with 84 atomic percent In/Zn were sputtered in 10 percent oxygen during deposition to produce highly resistive films. Resistive amorphous IZO films were annealed and characterized electronically and optically to determine the modifications made during annealing.

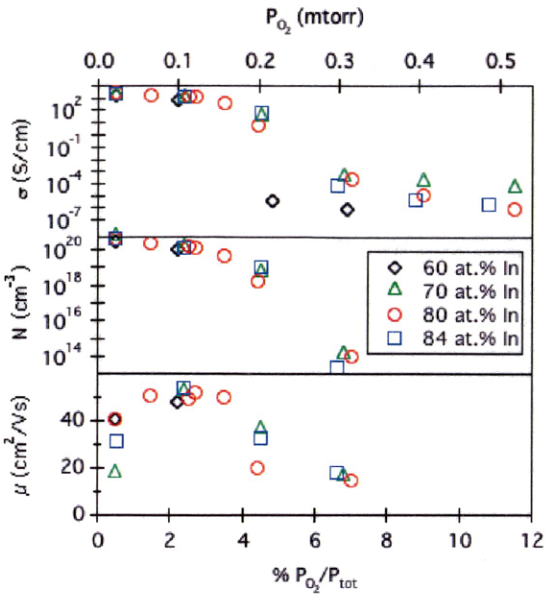

Figure 1.3 – Conductivity(σ), carrier concentration (*N*), and Hall mobility (μ) for various compositions as a function of oxygen content [4].

1.3.1 Bonding and Structure

IZO is composed of two oxide systems: indium oxide and zinc oxide. Indium oxide, In_2O_3, has the cubic bibixbite structure, a complicated 80 atom unit cell where indium has a six-fold coordination and oxygen 4-fold coordination. Zinc oxide, ZnO, exhibits the hexagonal wurtzite crystal structure, where the zinc atoms are nearly in position for hexagonal close packing. Every oxygen lies on a tetragonal site surrounded by 4 zinc atoms [18]. When combined together they form a range of compounds following $Zn_kIn_2O_{k+3}$ where k = 1 to 29 [2, 23, 24]. It is thought that by simultaneously depositing two structurally different metal oxides such as ZnO and In_2O_3 at low temperature, the resultant structural frustration yields an amorphous thin film materials over a relatively broad composition range [2, 25].

Since this study focuses on amorphous IZO it is important to understand how the bonds differ from normal semiconductors or metals. The outer shell electrons define the chemistry of the atomic element. In a periodic array of atoms, if there is overlap between outer shells, conduction of electrons is can occur. However, in an amorphous material

where there is no periodicity, outer shells have less overlap (bonds become directional) and carriers become less mobile. Many researchers have spent the last decade ascertaining why some materials can be amorphous yet stay conducting [26-28]. In this compositional range, seen in Figure 1.4, heavy metal cations with electronic configurations of $(n\text{-}1)d^{10}ns^{0}$, where $n \geq 4$, are able to conduct electrons through non-directional spherically symmetric *ns* orbitals because the overlap still occurs even in amorphous materials. Indium has an electronic ground state configuration of $[Kr]\ 4d^{10}5s^{2}5p^{1}$, but when bonded with oxygen becomes $[Kr]\ 4d^{10}5s^{0}$. In the case of zinc, the electronic ground state configuration is $[Ar]\ 3d^{10}4s^{2}$, and oxygen bonding alters the configurations to $[Ar]\ 3d^{10}4s^{0}$. Both indium and zinc have the correct bonding structure with oxygen to free *ns* orbitals making electrons available for conduction according this prediction.

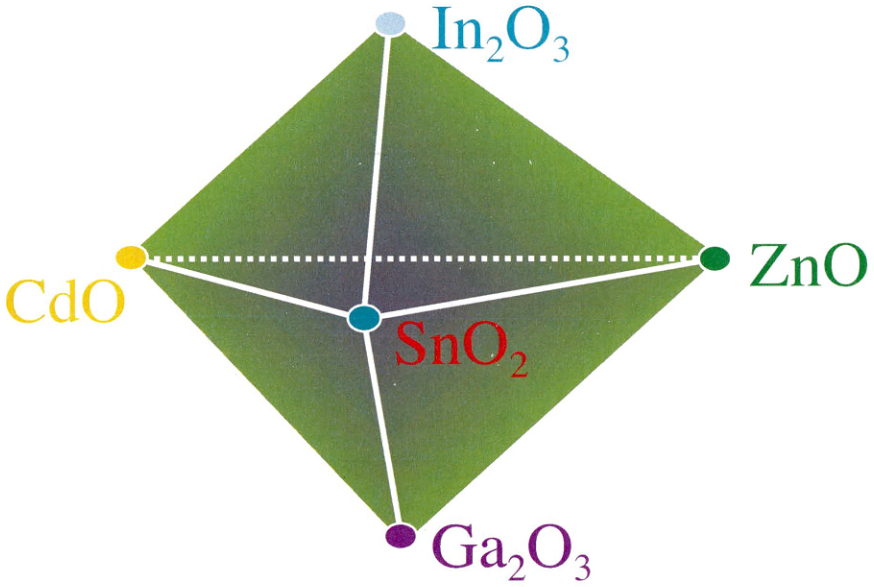

Figure 1.4 – Phase space of binary oxides being investigated individually and in compounds and alloys as novel and improved transparent conducting oxides (TCOs) [29].

1.3.2 Conduction and Bandgap

It is important to understand how In_2O_3 and ZnO obtain decent conduction of carriers based upon the bonding structure. In the defect-free state for either In_2O_3 or ZnO, the oxidation of In is 3+, Zn is 2+, and O is 2-, where all the lattice sites are

occupied. However, defects are introduced by changing the stoichiometry of films by increasing/reducing oxygen during deposition, or simply by vacancies, which occur naturally in all materials above absolute zero. One possible explanation is these defects introduce carriers into the material by freeing bonds. Both In_2O_3 and ZnO are n-type semiconductors, meaning they conduct electrons and not holes [18]. Using Kröger-Vink notation (a chemical equation of the physical system) [30], equations 1.1 and 1.2 illustrate how defects on the oxygen anion sites (rather than the metal cation sites) are typically observed to be the main contributors to carrier density in oxide materials.

$$ZnO \Leftrightarrow Zn_x + \tfrac{1}{2}O_{2(g)} + V_O^{\bullet\bullet} + 2e'$$

Equation 1.1

$$In_2O_3 \Leftrightarrow In_x + \tfrac{3}{2}O_{2(g)} + 3V_O^{\bullet\bullet} + 6e'$$

Equation 1.2

where a x indicates no doping, • is a positive charge, and ′ is a negative charge. Oxygen vacancies apply in single metal oxide systems, but in binary metal oxide systems one metal might end up as a dopant. For instance, if doping In_2O_3 by ZnO, IZO could be p-type and the carriers would be holes, as seen in equation 1.3.

$$\tfrac{1}{2}O_{2(g)} + 2ZnO \overset{In_2O_3}{\Leftrightarrow} 2Zn'_{In} + 3O_x + 2h^{\bullet}$$

Equation 1.3

Instead, when In_2O_3 and ZnO combine into IZO, they form an electrically conductive n-type conductor, which is highly dependant on the oxygen concentration [2-4, 18, 25, 31, 32], as in equations 1.1 and 1.2. Figure 1.5 shows that though there may be aliovalent doping of metal atoms indicated by the previous equations, it is oxygen vacancies that control conductivity. It must be understood that construct of Kröger-Vink notation is used as a physical representation of electronic properties in crystalline solids. IZO in this study is amorphous, and strictly speaking does not have lattice sites and actual oxygen vacancies. However, dangling bonds still exist, which allows the idea of doping to still apply in amorphous solids. A source for the loss of long-range order[10] is the frustration of the metal atoms by the difference in ZnO and In_2O_3 lattices, which when combined

helps to maintain the amorphous matrix state of IZO. Specifically, zinc is thought to frustrate the lattice of indium and stabilize the metastable amorphous state.

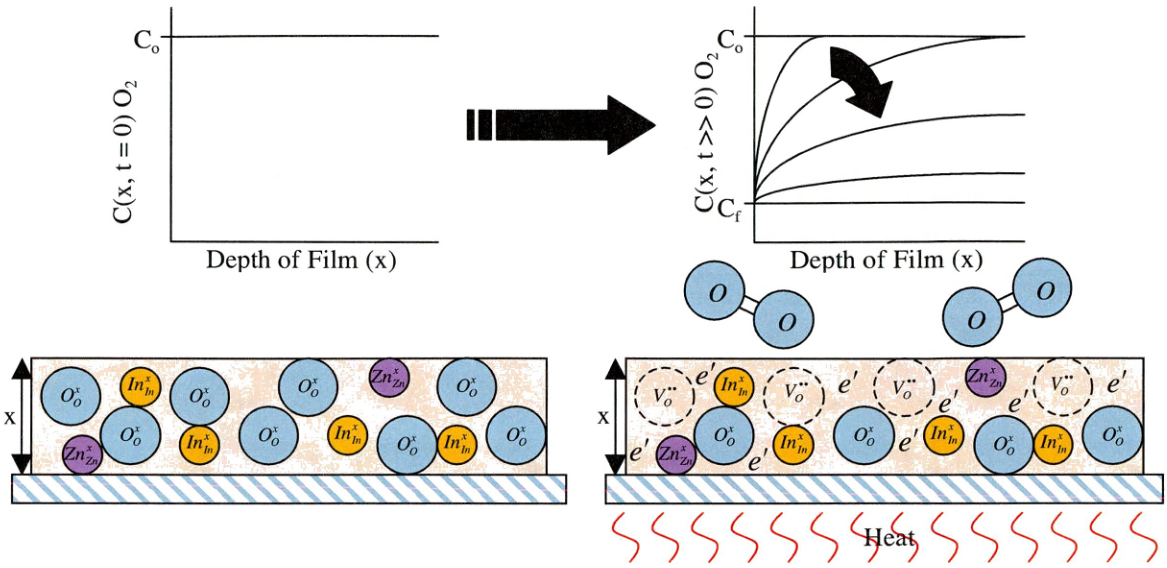

Figure 1.5 – A representation of an IZO film on glass with the concentration of oxygen decreasing when heat is applied. This figure incorporates equations 1.1 and 1.2.

Since materials in this study are amorphous, the concept of a parabolic band structure is not appropriate; well-defined crystal momentum depending on a periodic lattice cannot describe electronic states. Instead, the density of states versus energy, seen in Figure 1.6, is utilized to give an accurate depiction of the band structure. Unlike perfect crystalline materials, where the density of states is zero in the band gap, amorphous materials have mid-gap states. Mid-gap states are localized states, where carriers are trapped due to defects such as dangling bonds at states in between the conduction and valance band. The gap between the effective valance band and conduction band is called the mobility gap in non-crystalline solids. The mobility gap is defined by mobility edges [33, 34], quantifying the separation between localized and extended states. Localized states trap carriers, where extended states allow movement of carriers. The tailing of the bands into the mobility gap occurs due to the disordered structure of amorphous materials.

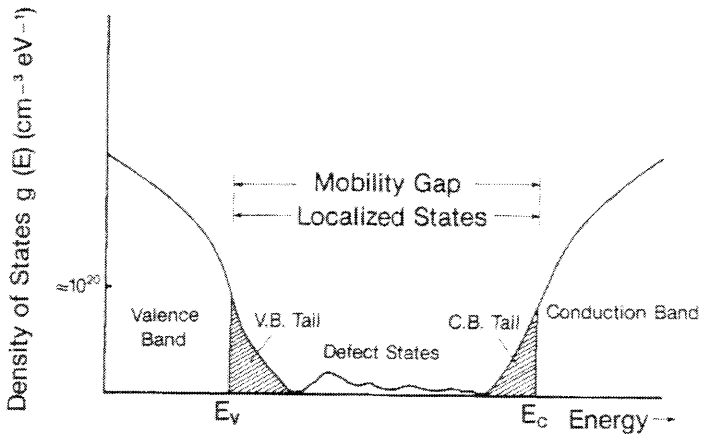

Figure 1.6 – Density of electronic states versus energy in a disordered solid [35].

1.3.3 Optical Properties

TCOs are important because of their ability to remain transparent in the visible wavelength spectrum of light, 400-700 nm or hν = 3.1-1.77 eV. Since many applications require optical transmission over the entire visible spectrum, TCO materials must therefore typically possess band gaps close to, or greater than, ~3 eV. This criteria level permits TCOs to be transparent until the ultra-violet spectrum is reached, where photons cause carrier across the bandgap. Absorption is held off at higher wavelengths until the energy of incoming photons approaches the plasma wavelength λ_p, where incident photons causing conduction electrons to be excited into an extended surface electronic excited states (free carrier absorption) called a surface plasmon resonance [36]. This wavelength indicates the amount of carriers free for conduction but λ_p decreases with increasing carriers. Even for very conducting TCOs, λ_p is in the infrared region. In between the two absorption regions, transparency is not 100 percent because extended tail states and mid-gap states of TCOs absorb some photons and allow carriers to be excited into other bands.

1.4 Thesis Organization

The rest of the thesis details our fundamental studies of low-temperature thermal instability in initially resistive IZO. The thesis organization is as follows: Chapter 2 goes into detail about the experimental techniques used and the theories behind the instruments and their operation. Chapter 3 provides literature background on previous a-InO, ZnO, and IZO conductivity/annealing studies, placing the current work into context. Chapter 4 contains the main results of this thesis, and represents a stand-alone archival paper that has been written for *Applied Physics Letters* describing the results of the experiments and new theories. In Chapter 5, additional results not explored in the journal paper will be discussed. Finally, in Chapter 6, conclusions and future work needed to further investigate IZO instability effects will be discussed at length.

CHAPTER 2 – EXPERIEMNTAL TECHNIQUES AND THEORY

An introduction to TCOs and the pertinent properties used to determine their characteristics was described in chapter 1. Also, the motivation for exploring the thermal instability in conductivity of α-IZO was rationalized. This chapter outlines the deposition and optical/electronic instruments used and their theories for analysis of the thermal instability.

2.1 Sputter Deposition

All IZO films were deposited in a vacuum chamber using DC magnetron sputtering. The sputtering process can be optimized to produce high quality, well-controlled composition films. Sputtering also produces very uniform films at high deposition rates without having to heat the substrate. Film properties can be tailored by flowing in reactive gasses, such as oxygen, hydrogen, or nitrogen during the sputtering process. In general, films deposited at room temperature tend to be amorphous, but by increasing substrate temperature, crystallinity and grain size improve [18].

Sputtering techniques require the use of a vacuum. In about 1640, Otto von Guericke designed the first piston-type vacuum pump, which he fashioned after the current day water pumps. In 1754, a little over a century later, Faraday sputtered the first films by using a glow discharge tube [37]. In 1935, Penning studied low-pressure sputtering on a glow discharge tube in the presence of a transverse magnetic field. The addition of a magnetron decreased the sputtering pressure and increased the deposition rate of films. Over the preceding years, fine tuning made DC magnetron sputtering a standard thin film deposition method of conducting oxides [18].

Sputtering is a physical vapor deposition technique used to deposit a variety of metals and alloys and a number of compounds. There are many sputtering processes but in this study only DC magnetron sputtering was used. The sputtering technique requires

a suitably low vacuum pressure (typically < 10^{-6} torr) to remove contaminates to provide a clean homogenous film. Once the chamber is evacuated inert gasses, usually argon (Ar) or xenon (Xe), are introduced to a desired pressure to operate the magnetron.

Once the magnetron is on, a potential (usually ~300V) is produced between the target, negative, and substrate. Positively charged gas ions bombard the surface of the target due to the potential and cause primary recoil atoms to redistribute their energy by cascade collisions with surrounding atoms. If the ballistic impact has energy greater than the ~3 times binding energy (approximately equal to the heat of sublimation) of the target material, an energy transfer occurs and target atoms are ejected from the surface of the target [38]. Target atoms travel unhindered on a ballistic trajectory to a surface and stick. Sputtering is wasteful and expensive because the substrate is not the only surface deposited on. If the target atoms are charged, and electric field can direct the atoms to the substrate. A film can be grown of desired thickness by knowing the film growth rate and choosing the correct sputtering time.

Aside from the sputtering process, an important secondary effect is the release of electrons from the target. These electrons can collide with the inert gas molecules ionizing the gas generating more ions for sputtering. This process helps to sustain the glow discharge plasma during sputtering.

The addition of a magnetic field through a magnetron placed behind the target localizes free electrons thereby increasing the number or interactions with the inert gas to produce even more ions. An increase in ions is directly correlated to an increase in the density of the plasma, thus an increase in deposition rate [39]. Also, the magnetron reduces the required pressure because of the increase in the density of the plasma.

One disadvantage to the magnetic field is the preferential collision ring, or racetrack, created on the target by ion bombardment, seen in Figure 2.1. The racetrack renders much of the target material wasted unless reclaimed. The racetracks are caused as electrons are accelerated away from the gun due to the electric field and simultaneously they are also accelerated in a spiral path due to the magnetic field from the magnetron. This behavior is caused by the Lorentz force from just the magnetic field and is given by

the equation [40]

$$\vec{F} = \vec{F}_E + \vec{F}_B = q_e(\vec{E} + v \times \vec{B})$$

Equation 2.1

where $\vec{F}_E$ is the force on the electron due to the electric field, $\vec{F}_B$ is the force on the electron due to the magnetic field, $\vec{E}$ is the electric field, $\vec{B}$ is the magnetic field, q_e is the charge of electron, and v is the velocity of electron. The racetrack signifies the area where increases in free electron concentration create more ions, which in turn increases the number of collisions and plasma density.

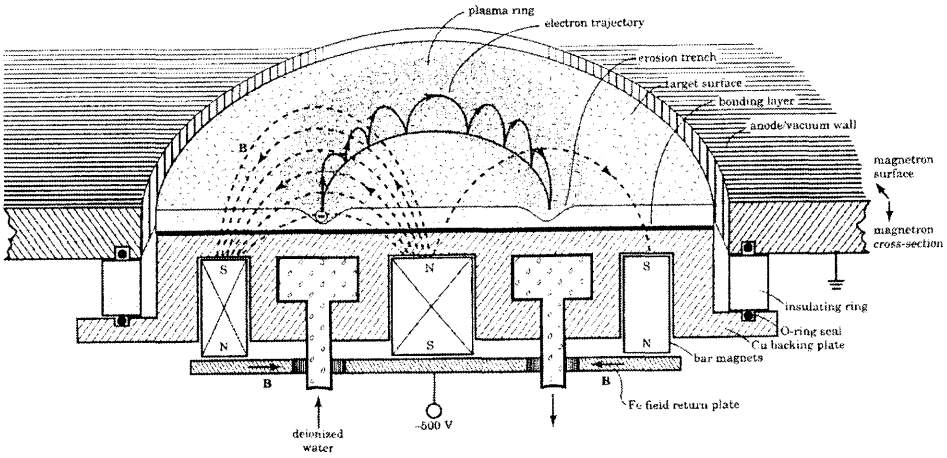

Figure 2.1 – Illustration of a magnetron showing the magnetic field and path of electrons [41].

α-IZO thin films are produced on 5.08 x 5.08 cm Corning Eagle 2000 glass substrates using DC magnetron sputtering. Sputtering target to substrate distance is approximately 11 cm. The substrate glass is cleaned with Alconox, then rinsed with deionized water. 5.08 cm circular sputtering targets from Plasmaterials are used with a composition of 84/16 atomic percent In/Zn. The sputtering chamber is pumped down to a pressure < $5x10^{-6}$ torr using a turbomolecular pump. A ratio of 90/10 percent argon to O_2 is employed with a sputter pressure of 4.5 mtorr in the chamber at a 40 W power setting, or 2 W/cm^2 normalized at a distance of approximately 11 cm. An Advanced Energy MDX 1.5K power supply is used with an Advanced Energy Sparc-le 20 to prevent arcing.

Samples are deposited vertically downward with 10 percent O_2 to produce a highly resistive beginning state, $\sigma \sim 10^{-4}$ S/cm. During the deposition process a "burn-in" was always performed to avoid thermal shock and to sputter away contaminants in the surface oxide before opening the shutter [4].

2.2 Electrical Characterization

This section describes the custom setup designed to measure the thermally activated persisted electrical conductivity. The electrical properties of α -IZO were measured using four-point probe. The theory behind four-point probe is discussed at length.

2.2.1 System Setup

A new system setup was required to take four-point probe measurements while heating the sample. This new setup will enable data logging of the time dependent thermal instability characterized by four-point probe. A schematic of the instrument is presented in Figure 2.2. Samples are positioned on a ULTARMIC 600 2.54 x 2.54 cm ceramic heater clamped to ceramic inserts to decrease heat loss to the surroundings. A Eurotherm 2416 acts as the heater control through a K-type thermocouple, which contacts the front surface, thus the film, of the sample being heated. S-750 Micropositioner probes from Signatone measure the electrical properties of the sample under different test runs. A cardboard box covered in aluminum foil and aluminum tape covers the heater and micropositioners to isolate the system from light because of photoconductive instabilities in amorphous IZO films. LabVIEW 8.2 visual programming code controls the setup by measuring and controlling voltmeters, electrometers, and source meters. Internal impedance of the voltmeters are within an order of magnitude of the samples; therefore, electrometers are used. A Keithley 619 electrometer has an internal impedance of ~20 TΩ and the samples reached a maximum of ~10 GΩ, a difference of approximately three orders of magnitude.

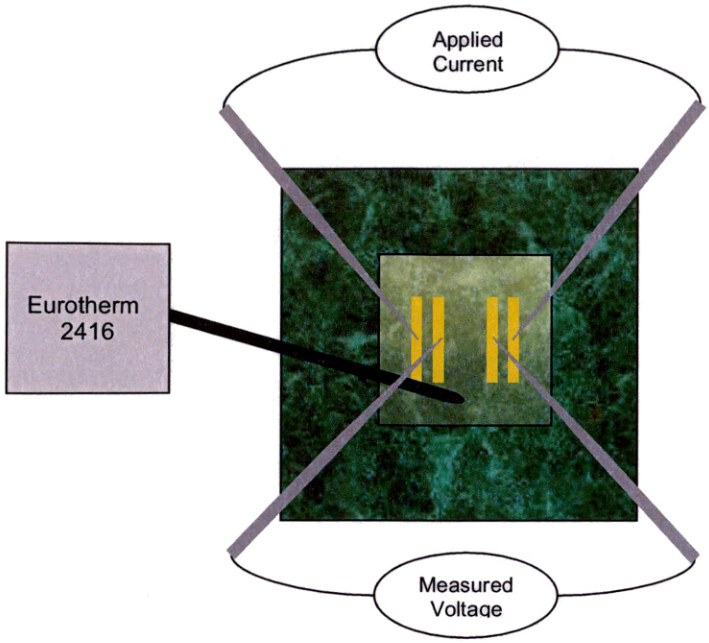

Figure 2.2 – Schematic of setup: ULTRAMIC 600 heater (green), probes (grey), thermocouple (black), contact pads (yellow).

2.2.2 Four Point Probe

The four point probe method was developed by Valdes in 1957 to make resistivity measurements on Germanium transistors. The method uses four sharp probes in line on a flat surface where the outer probes pass current and the inner electrodes measure the resulting voltage drop [42]. This method assumes both a semi-infinite flat solid, limiting the current path, as well as a semi-infinite volume.

$$\rho = \frac{2\pi}{\left(\frac{1}{s_1} + \frac{1}{s_3} - \frac{1}{s_1 + s_2} - \frac{1}{s_2 + s_3}\right)} \frac{V}{I}$$

Equation 2.2

where ρ is resistivity, ohm-cm, V is the voltage drop across inner probes, I is the current driven through outer probes, and s_1, s_2, s_3 are probe spacing, cm. If the spacing between probes is equal equation 2.2 can be reduced to equation 2.3

$$\rho = 2\pi s \frac{V}{I}$$

Equation 2.3

However, when looking at thin films (t/s is <= 0.5 where t is the thickness of film, in cm),

which do not have a semi-infinite volume as in the above equation, the thickness with a correction factor (a = 0.72 t/s) must be considered [43, 44].

$$p = a2\pi s\frac{V}{I} = 4.53t\frac{V}{I}$$

Equation 2.4

There are also correction factors that must be considered, when making measurements, depending on the specific sample geometry. In the four point probe setup used, contact is made on Ti/Au pads ~200/2100 Å thick deposited by vacuum evaporation, seen in Figure 2.3. Contacts were produced in such a fashion to reduce the difficulty of manually placing probes onto the sample. Normal four point probes are collinear and not on conductive pads like the setup built. Therefore, the geometry of my setup is taken yielding equation 2.4.

$$p = \frac{ht}{S_2}\left(\frac{V}{I}\right)$$

Equation 2.5

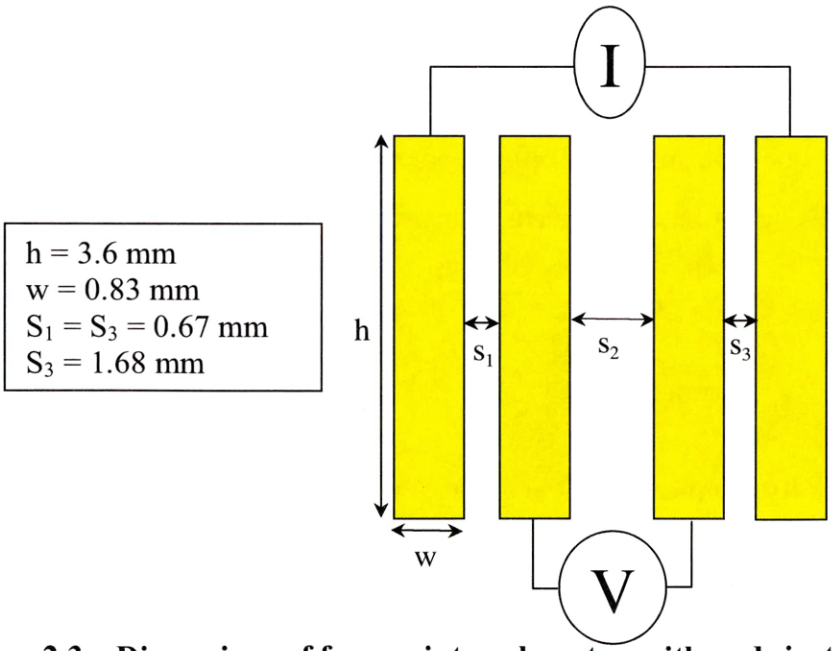

Figure 2.3 – Dimensions of four-point probe setup with pads instead of points.

There are a number of sources in error when using a four-point probe system. Ultimately, it was decided that the error in measurements due to the unique geometries

used was much less than the order of magnitude change seen. Therefore, without corrections this system focuses on relative measurements rather than absolute. Some situations where corrections are needed are discussed further. Correction factors should be employed when current spreading becomes a problem with point contacts. The current does not always follow the path of least distance, but rather follows the field lines created by the potential difference required to drive the current though the film. In normal collinear four-point probe measurements current spreading can be a large source of error requiring correction factors. However, with different geometries current spreading may not be as large a concern. Geometric correction factors also arise when the thickness of the film is comparable to the spacing of the probes, as mentioned before a = 0.72 t/s when t/s is <= 0.5 where t is the thickness of film for collinear probes. Since the resistivity of the samples changed by orders of magnitude, importance was placed on the relative change rather than absolute value of the measurement. Therefore, correction factors for current spreading and geometry, including sample thickness, were ignored for this setup. Other correction factors can be found in references [42-46].

Often when evaluating electrical characteristics, sample conductivity is used. Conductivity measures the relative ability of a material to accommodate the flow of charge. Conductivity depends on carrier concentration (N) carrier charge (e) and carrier mobility (μ) as:

$$\sigma = Ne\mu$$

Equation 2.6

Conductivity has a simple inverse relationship with resistivity.

$$\sigma = \frac{1}{\rho} = \frac{S_2}{ht}\left(\frac{I}{V}\right)$$

Equation 2.7

where σ is conductivity, S/cm. When evaluating highly resistive materials, contact and spreading resistance can play a large role in measurement error. The four-point probe method is therefore widely used because it negates issues with contact and spreading resistance. The few drawbacks to the four-point probe method are the potential to cause

damage to the sample through indentation from probes, and sampling a relatively large area on the sample, preventing high-resolution measurements [46]. A correction factor ultimately was not used due to the large magnitude change in measurements. Using the four-point probe method provides relative measurements of the conductivity of these samples during heating, as seen in Figure 2.3.

2.3 Optical Characterization

Optical characterization is imperative to understanding how transparent conducting oxides behave. Techniques such as, transmission and reflection can be used to measure the band gap. Other optical methods, like ellipsometry, can be used to simply measure the thickness of films.

2.3.1 Spectroscopic Ellipsometry

After the films are deposited in the sputtering chamber, an ellipsometer determines film thickness quickly and easily. In the case of this study, IZO film thickness measurements are conducted using an α-SE spectroscopic ellipsometer from J.A. Wollam Co., Inc.

The first documented instruments that can be called ellipsometers came from back in 1808/1809 from Malus and in 1814 from Brewster [47]. However, it was Drude, in 1887, who first developed the equations of ellipsometry. Drude is well known for his 'Drude Model', which describes the electronic properties of metals. Until the 1970s, most ellipsometers were very slow and had to be operated manually. Since 1990, photodiode arrays (PDA) were utilized to make multi wavelength scans possible, creating spectroscopic ellipsometers [48].

Ellipsometry is a non-destructive optical measurement which probes a sample with oblique polarized light. Upon reflection, the polarization of the light often becomes 'elliptical,' hence the origin of the name ellipsometry. Ellipsometry measures the change in polarization state of the light after reflection characterized by Psi(ψ) and Delta(Δ).

$$\tan(\psi)\cdot e^{i\Delta} = \rho = \frac{r_p}{r_s}$$

Equation 2.8

where *tan(ψ)* is the magnitude of the reflectivity ratio, Δ is the phase, and ρ is the ratio of reflectivity of polarized light (r_p) to reflectivity of s-polarized light (r_s). Because ellipsometry uses a ratio of polarized light, the absolute intensity of the light beam is not important as it is in other measurements (such as transmission and reflection). The fact that ellipsometry measures two values (ψ and Δ) as a function of wavelength provides more information than is provided by the intensity as a function of wavelength data produced by either transmission or reflection measurements. Another great feature is Δ provides enough sensitivity to yield sub-nm precision in thickness measurements. Ellipsometry also has a major advantage in that scans are very fast, taking only a few seconds, and thus allowing the possibility of real-time measurements [49].

The only major drawback to using ellipsometry is the versatility provided by ψ and Δ as a function of wavelength makes data analysis complicated. To extract values such as sample thickness and optical constants, an optical model must be used to fit the data. Specifically, to fit transparent thin films, the Cauchy dispersion relation is used in modeling [49]. The Cauchy dispersion relation determines the index of refraction 'n' as a function of wavelength.

$$n(\lambda) = A_n + B_n/\lambda^2 + C_n/\lambda^4$$

Equation 2.9

Where n is the wavelength dependant index of refraction, λ is the wavelength of interest, A_n is a parameter related to average index of refraction of material, and B_n and C_n are parameters related to the shape or curvature of the dispersion curve as a function of wavelength. IZO sample thickness is determined using model fitting with a spectroscopic ellipsometer. Spectroscopic ellipsometry modeling can also determine electrical properties using the refractive index. Note, modeling is difficult for amorphous materials, due to phase separations, gradients in composition, and film roughness. Even though

spectroscopic ellipsometry was used to determine IZO sample thickness, transmission and reflection is utilized as an additional optical technique to provide further insight into electronic properties. Thickness was measured by a spectroscopic ellipsometer due to ease and convenience; however, a profilometer could have been used just as easily.

2.3.2 Reflection and Transmission

Reflection (R) and transmission (T) is an important tool used to characterize TCOs. Light from UV/Visible lamp is focused to < 1mm spot size, important for obtaining R and T data between contact pads on the films, from a fiber optic cable coupled with two Ocean Optics CCD array spectrometers, which cover the full spectral range measured. Transmission spectra was normalized to substrate transmission. The substrate was Corning Eagle 2000 glass. Reflection spectra was normalized to a standardized aluminum mirror.

Both electronic and optical properties may probed by reflection and transmission. Photons, which are not transmitted, are either absorbed or reflected. The principle optical feature of TCOs is high transmission in the visible portion of the spectrum (450-750 nm). Absorption of photons at high energies is indicative of the bandgap, where photons excite carriers into higher conduction bands. At lower photon energies, the plasma wavelength may be determined, where absorption and reflection increase again. The plasma wavelength is the wavelength at which free conduction electrons in a solid coherently resonate in response to an incident electromagnetic wave. Since all samples in this study are extremely resistive, thus pushing the plasma wavelength into the far infrared, it is prohibitively difficult to differentiate between intrinsic free carriers and phonon effects which increasingly occur at longer wavelengths.

A representative plot of reflection (R) and transmission (T) for an amorphous IZO film is shown in Figure 2.4. The oscillations in R and T are interference fringes. Their spacing is a function of the mismatch of index of refraction of the film (n= 2.1) and Eagle 2000 glass (1.5) and film thickness. These films are highly transparent at $\lambda > 500$

nm, below which the films begin to absorb and is why α-IZO has a yellow green tint to it.

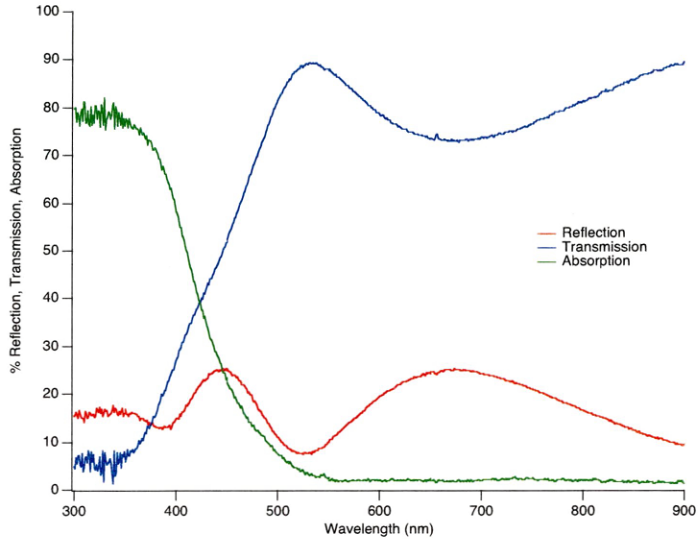

Figure 2.4 – Typical reflection, transmission, and absorption spectra of an IZO thin film.

The absorbance of the film is estimated from reflection and transmission A=1-T-R and the absorption coefficient, α, is utilized to estimate the optical bandgap.

$$\alpha = \frac{4\pi k}{\lambda}$$

Equation 2.10

where k is the imaginary part of the complex index of refraction and λ is the wavelength of interest. Reflection , transmission , and absorption coefficient are related by

$$T = \frac{(1-R)^2 e^{-\alpha t}}{1-R^2 e^{-\alpha t}}$$

Equation 2.11

where t is the film thickness, and R is the single reflection from air-film interface which is about one half the measured reflection, $\tilde{R}$. Expanding equation 2.11 yields

$$T = \frac{(1-2R-R^2) e^{-\alpha t}}{1-R^2 e^{-\alpha t}}$$

Equation 2.12

If the product of αt is large or R is small then the denominator reduces to 1 [2] and R^2

drops out and the absorption coefficient may be extracted as

$$\alpha = \frac{-\ln\left(\frac{T}{1-\tilde{R}}\right)}{t}$$

Equation 2.13

where $\tilde{R}$ has been substituted in for 2R. The approach to modeling the optical bandgap, E_{opt}, assumes a direct bandgap of materials with parabolic energy bands and a uniform refraction index and approximates the absorption coefficient as

$$\alpha = \left(\frac{e^2(2m_r)^{\frac{3}{2}}}{Nch^2m_e^*}\right)(h\nu - E_{opt})^{\frac{1}{2}}$$

Equation 2.14

where m_r is the reduced carrier mass, h is Planck's constant, and ν is the photon frequency [50]. Note that the assumption of parabolic energy bands in not correct in amorphous materials where band tail states are common. Therefore, the absorption coefficient is not accurate across the whole bandgap. Nevertheless, an effective optical band gap, E_{opt}, is obtained by extrapolating the linear portion of equation 2.14 squared tp $\alpha^2 = 0$, seen in figure 2.5.

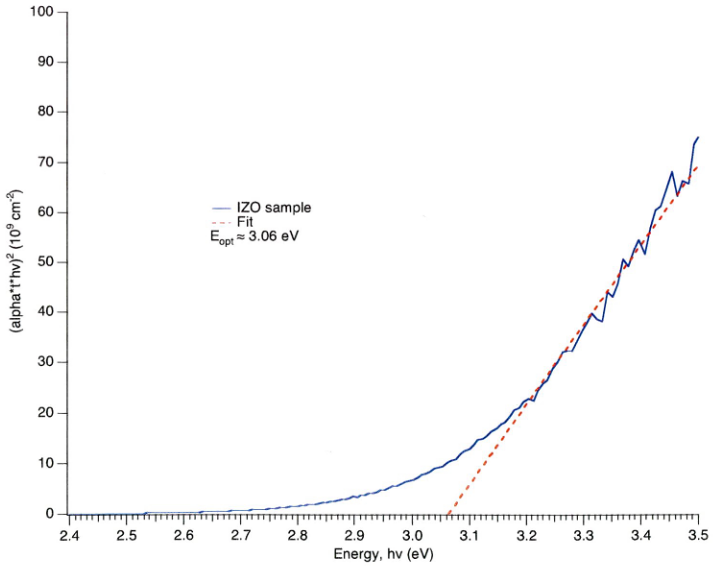

Figure 2.5 – Absorption plot is fit and x-intercept provides the optical bandgap.

2.4 Structural Characterization

Before and after annealing the samples, structural tests are conducted to verify if there are any structural changes. There are many different possible ways to determine the structure of a sample; however, not all techniques focus on the same aspects and delve into the same qualities. For example, x-ray diffraction (XRD) is very important to crystalline materials, but in amorphous materials more care is required to obtain quality information on the structure. Even though XRD may not be optimized for amorphous materials, it may uncover crystallization or local reordering effects after annealing. This section investigates the different techniques utilized in this study.

2.4.1 X-Ray Diffraction

X-ray diffraction (XRD) is an essential characterization tool for examining any crystalline solid. XRD is particularly useful in characterizing single crystalline, polycrystalline, and powdered materials. In 1912, a German physicist by the name of von Laue brought the current theories of x-ray wavelengths, ~1-2 Å, and crystal unit cells, ~1-2 Å on a side, together. He took a crystal of copper sulfate and set it in the path of a narrow beam of x-rays and a photographic plate and produced the first ever X-ray diffraction pattern. Later that year Bragg, an English scientist, analyzed the experiment by von Laue and was able to simplify the mathematics into the form known today as Bragg's Law [51].

$$n\lambda = 2d\sin(\theta)$$

Equation 2.14

Bragg's Law states the essential condition that must be met in order for diffraction to occur. λ is the wavelength of the incident x-ray on the sample. λ is usually a Cu Kα x-ray, at 1.54 Å. d is the distance between similar planes of atoms. θ is the angle at which the reflected x-ray travels at from the plane of the sample. n is the order of the diffraction, an integer number of wavelength differences between diffraction planes. Figure 2.6 illustrates the path and x-ray takes during diffraction. As incident x-rays cause

constructive interference with whole numbers of n, the signal is collected by a detector and changes as a function of θ.

The IZO films in this experiment are amorphous instead of crystalline. Instead of clear diffraction peaks at specific wavelengths, a broad hump characterizes amorphous films. XRD is utilized before and after annealing to discover if any crystallization has begun at the annealing temperatures used. Another hope for XRD was to see small changes in the amorphous peak region, indicating a small structural order change, which might explain the electric properties seen in IZO after annealing. To obtain such small changes, it can be beneficial to deposit the amorphous material in question on crystalline silicon to compare the changes of the amorphous peak.

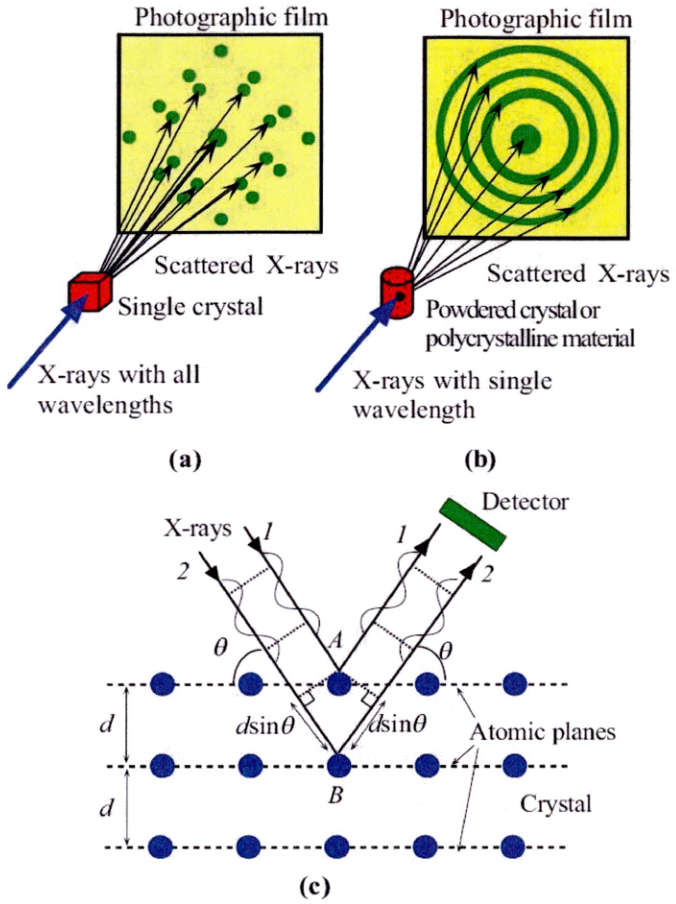

Figure 2.6 – Diffraction patterns obtained by passing X-rays though crystals can only be explained by using ideas based on the interference of waves. (a) Diffraction of X-rays from a single crystal gives a diffraction pattern of bright spots on a photographic film. (b) Diffraction of X-rays from a powdered crystalline material or a polycrystalline material gives a diffraction pattern of bright rings on a photographic film. (c) X-ray diffraction involves the constructive interference of waves being "reflected" by various atomic planes in the crystal [52].

2.4.2 Temperature Programmed Desorption

Temperature Programmed Desorption or TPD is a technique used to examine what gasses desorb from the sample surface as a function of temperature. In the experiment, a few milligrams of the sample are placed inside an empty glass tube under vacuum. The surface is first exposed to a gas at a particular temperature to obtain a specific initial coverage. The surface is then heated in a controlled manner so that the gas desorbs. The gas pressure above the surface is monitored as the surface is heated. The competition between molecules entering the gas phase volume through desorption and leaving the volume through pumping of the experimental chamber creates a pressure spectrum with a characteristic shape [53]. The temperature is ramped up at a linear rate and the gasses are measured with a quadrupole mass spectrometer (QMS). Once the scan is finished, results are compared to a database of masses to determine at what temperature and time a species of gas desorbed from the film. The theory behind the desorption kinetics are not relevant to this thesis but can be accessed through reference [54].

TPD was used as a characterization technique in order to reveal the details behind and absorption or desorption taking place in the IZO film, specifically looking at oxygen. Oxygen is important because if it is desorbing, oxygen vacancies are left behind which release two electrons per vacancy. Conductivity of the film will increase providing an explanation for the annealing phenomenon.

CHAPTER 3 – PREVIOUS EXPERIMENTAL WORK

Chapter 3 describes previous experimental work performed on indium zinc oxide. Detailed inspections of interactions between indium, zinc, and oxygen, structural changes with temperature, and electrical property transformations during annealing are explored here.

3.1 Structural Changes With Temperature

It is important to identify the temperature at which crystallization of amorphous IZO occurs during annealing, because the electrical properties depend heavily on oxygen vacancies and structure. Jung et al. [1] used differential thermal analysis (DTA) to discover the crystallization temperature by using amorphous IZO on a silicon wafer. They, as well as others [2, 55], discovered the crystallization temperature of their IZO, 90/10 wt. percent In/Zn, to be between 500 and 600 °C, which is seen in Figure 3.1. Gonçalves et. al [56] annealed films possessing the same 90/10 wt. percent In/Zn composition while tracking the oxygen partial pressure desorbed from the thin film using an RGA. They discovered three peaks, as seen in Figure 3.2, which corresponded to weakly bound oxygen (~600 K), In_2O_3 releasing oxygen (~875 K), and ZnO releasing oxygen (~ 950 K) respectively. It is interesting to note that the crystallization of IZO at 500 to 600 °C seen by Jung et al. coincides approximately with the two peaks observed by Gonçalves et al. at ~900 K (~600 °C). It has been suggested substituting Zn^{2+} "sub-lattice" of ions increases the energy barrier for the diffusion of atoms, sustaining the amorphous structure [1, 4, 25, 55]. At lower temperatures, this would be true because of the structural frustration of cubic bibixbite structure (exhibited by In_2O_3) and hexagonal wurtsite (exhibited by ZnO) structure.

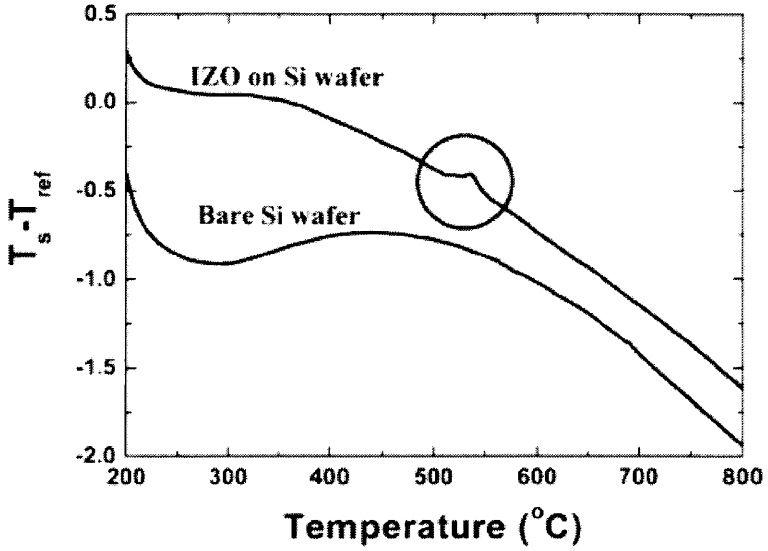

Figure 3.1 – DTA curves of a bare silicon wafer and an IZO thin film deposited on silicon wafer [1].

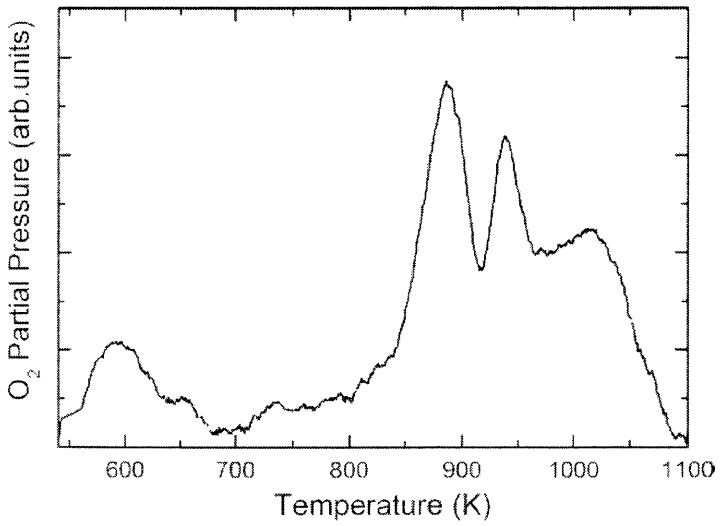

Figure 3.2 – Oxygen exodiffusion spectra of IZO films [56].

This hypothesis is also supported by research from Taylor et al. [2, 57]. Taylor focused on the complete composition range of IZO from pure indium oxide to pure zinc oxide in their studies on annealing. In Figure 3.3, they show that no crystallization occurred in the amorphous region of IZO (< 84% In/Zn), even as high as 500-600 °C. As atomic percent of indium is increased, crystallization peaks from XRD show up at lower temperatures, seen in the 87 percent and 89 percent indium content graphs. However, as Taylor et al. illustrate in Figure 3.4, films between 45 and 85 at. percent indium stay amorphous even after annealing to 600 °C for one hour in an Ar atmosphere. The top graph indicates that the full width half maximum (FWHM) of the amorphous peak is broader than that of the crystalline peak. It is also important to note the lattice spacing (d) of amorphous IZO conforms more closely to the ZnO lattice spacing than to In_2O_3, as shown in the bottom graph. This observation suggests the structural frustration caused by the hexagonal wurtzite lattice preserves the amorphous state.

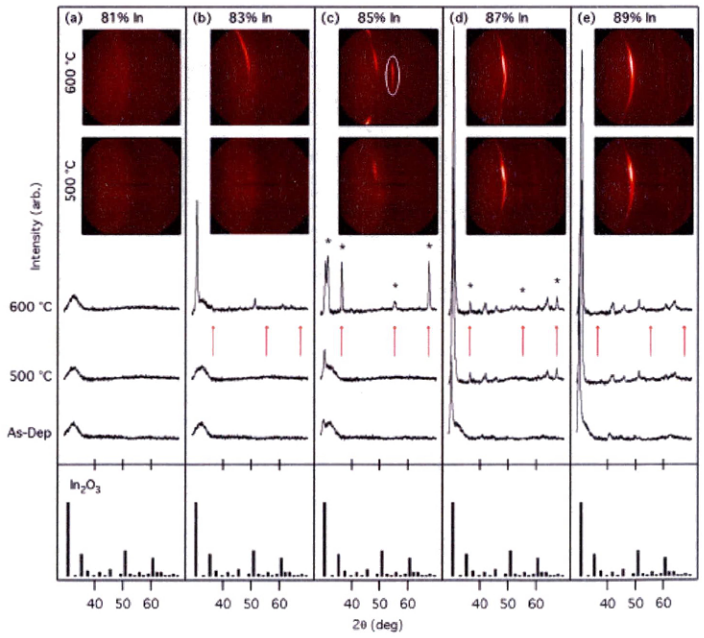

Figure 3.3 – Crystallization of amorphous IZO. X-ray diffraction spectra showing the amorphous to crystalline transformation. The x-ray diffraction spectra for the as-deposited, 500 and 600 °C air annealed compositions from 81 to 89 at. percent In (L4, columns 3 to 7). The insets show the detector images using a common linear color scale for IZO annealed in air at 500 and 600 °C [57].

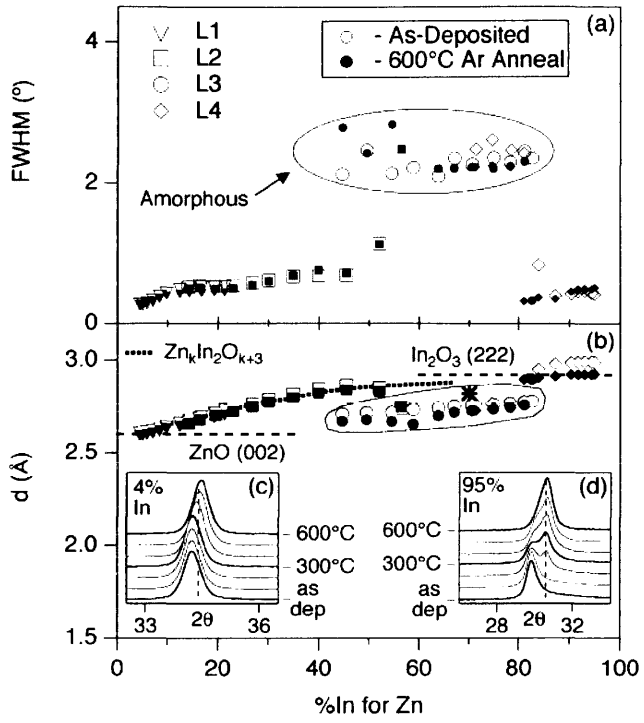

Figure 3.4 – Analysis of the X-ray diffraction spectra. The full width at half maximum (FWHM) (Panel (a)) and the d-spacing (Panel (b)) for as-deposited and 600 °C argon annealed IZO as a function of indium content. The horizontal, dashed lines in the bottom panel indicate the d-spacing for ZnO (002) and In_2O_3 (222). Panels (c) and (d) show the spectra after annealing at various temperatures for IZO 4/96 and IZO 95/5 respectively. The vertical dashed lines in the insets show the 2θ positions for ZnO (002) (Panel (c)) and In_2O_3 (222) (Panel (d)). The * symbol in the Panel (b) at 70 at. percent In is the nearest neighbor spacing as determined from a TEM electron diffraction pattern and it agrees well with XRD data. In Panel (b), the dotted line shows the effective ZnO d 002 layer spacing of the $Zn_kIn_2O_{k+3}$ homologous compounds [31].

3.2 Annealing for Electrical Properties

Post-deposition annealing of TCO films frequently improves mobility and enhances electrical properties [18]. The short-range order of amorphous TCOs may improve by annealing, which reduces scattering of charge carriers, increasing mobility. Due to the remarkable thermal stability of IZO, films may be annealed up to 500 °C before the appearance of a crystalline phase, depending on composition [57].

One of the first annealing studies on IZO was completed by Major et al. in 1984 [58]. In this study, spray deposited crystalline zinc oxide doped with 0-2 percent indium was annealed (up to 600 °C) in three different environments: oxygen, air, and vacuum. The gross effects of annealing in oxygen and air were similar. The overall encompassing effect noted in this paper is when annealing in oxygen or air, the resistivity increased drastically, while subsequent anneals in vacuum reduced resistivity. All the films were seen to follow this effect. This paper explored the Zn-rich region of IZO (almost purely ZnO), while the studies presented in this thesis focus on the indium-rich region of IZO (90/10 wt. percent In/Zn). Interestingly, however, this oxygen sensitivity effect is seen by both Kim et al [59] and Barquinha et al [60] with high indium content as well.

Electronic properties of IZO thin films are dominated by the thermodynamics and kinetics of the absorption and desorption of oxygen. Films with substantial oxygen deficiency initially possess large concentrations of oxygen vacancies, whereas oxygen vacancies concentrations can be strongly suppressed in films initially containing excess oxygen. This fact has strong implications on the electronic behavior of IZO and can be conceptualized in Kröger-Vink notation [61].

$$ZnO \Leftrightarrow Zn_x + \tfrac{1}{2}O_{2(g)} + V_O^{\bullet\bullet} + 2e'$$

Equation 3.1

$$In_2O_3 \Leftrightarrow In_x + \tfrac{3}{2}O_{2(g)} + 3V_O^{\bullet\bullet} + 6e'$$

Equation 3.2

where a x indicates no doping, • is a positive charge, and ′ is a negative charge. Once again, Kröger-Vink is for crystalline solids; however, amorphous IZO does not have lattice sites or actual oxygen vacancies, but it can demonstrate the change in electrical

properties of amorphous materials. Because the initial oxygen concentration in these films may not be representative of the thermodynamically stable condition in a given oxygen environment, annealing these samples at sufficiently high temperatures, as discussed by Gonçalves et al. [56], can lead to a restorative increase or decrease in the oxygen vacancy concentration of the film as it achieves a thermodynamic balance with its environment. For example, annealing an excessively oxygenated film in a vacuum will cause desorption of oxygen, thereby increasing the film conductivity by the creation of oxygen vacancies and free electrons. On the other hand, annealing in an oxygen rich environment will allow oxygen to absorb into the film annihilating oxygen vacancies, localizing electrons to oxygen bonds and thereby reducing the overall conductivity of the film.

It is interesting to note these observed annealing effects are somewhat reversible. Subsequent anneals at sufficiently high temperatures in oxygen environments and then in vacuum will reverse the electrical characteristics of IZO films, but not completely. This effect can be seen in Figure 3.5(a), where Kim et al. [59] anneal in vacuum a highly resistive sample (curve 1), decreasing resistance by delocalizing electrons and allowing oxygen to desorb. Upon cooling (curve 2), oxygen stoichiometry is static until the sample is annealed in an air environment (curve 3) increasing resistance by permitting oxygen absorption. Finally, the sample is annealed in vacuum (curve 4) once again decreasing resistance.

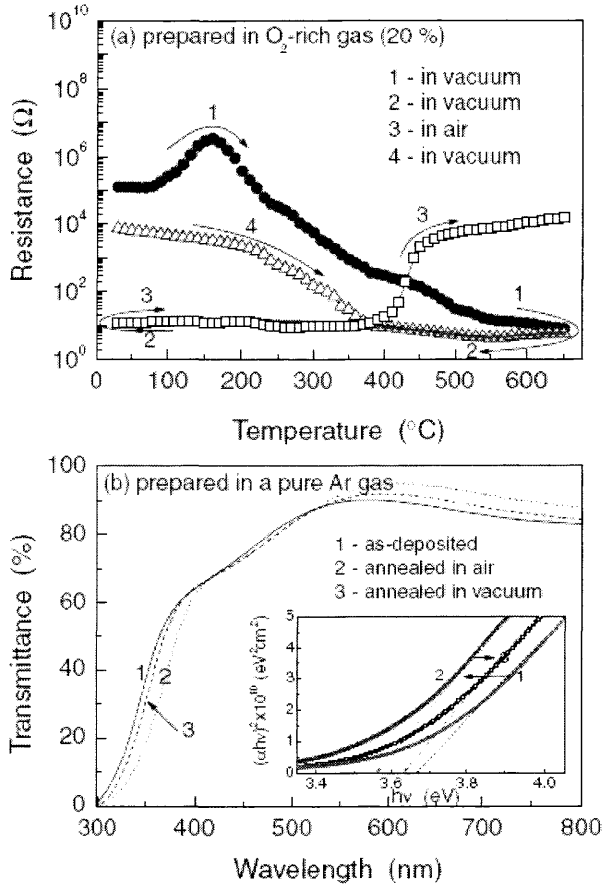

Figure 3.5 – (a) Electrical resistance changes during the cyclic heat treatments from RT to 650 C for IZO film deposited in an oxygen concentration of 20 percent. (b) Transmission spectra (a) before and (2) after the heat treatment in vacuum, and (3) after the heat treatment in air for the film heated in vacuum, when the as-deposited film is prepared in pure argon gas [59].

In amorphous indium oxides (α-In_2O_3), resistivity is also seen to decrease by orders of magnitude upon heating at low temperatures (150-180 °C) as demonstrated in Figure 3.6 [62]. This effect is due to both heating and persistent photoconductivity in α-In_2O_3. However, the α-In_2O_3 is observed to stabilize in a crystalline phase after heating. Studies on α-In_2O_3 studies attribute the resistive changes to an oxygen diffusion process that is thermally or photonically activated [62, 63]. α-In_2O_3 is similar to α-IZO, because it also has a photoconductivity effect demonstrated in TTFTs [11]. Also, crystalline IZO exhibits a large change in conductivity due to heating in various atmospheres [58-60]. This thesis explores the retention of the amorphous IZO structure while maintaining large increases in conductivity. As previously suggested, the mixing of the two crystalline structures of In_2O_3 and ZnO frustrate the local structure such that the amorphous state persists.

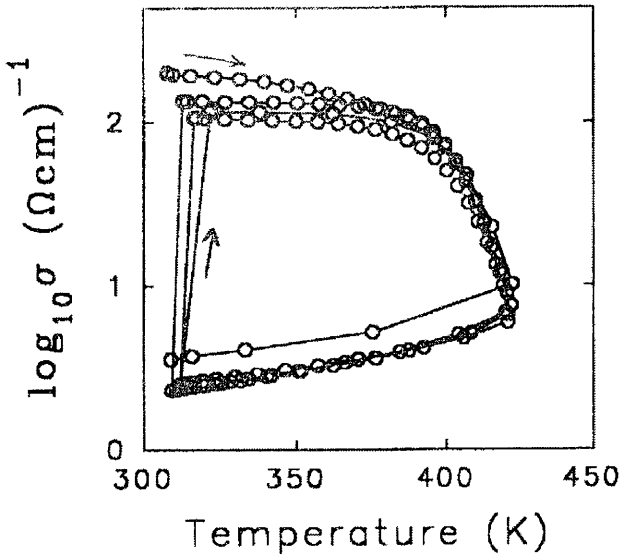

Figure 3.6 – Temperature cycling to 420K in vacuum decreases σ while UV light exposure for 40 min at 310K increases σ. Three cycles are shown. Sample was 25 nm thick sputtered with P_{O_2} = 1 mTorr [62].

Optical property variations in TCO films can often be directly correlated to what is happening electronically in the films. Figure 3.5(b) demonstrates a shift in reflection and transmission occurring during annealing at 650 °C in vacuum and oxygen. A shift in the absorption edge occurs from the as-deposited sample to air-annealed sample (Red shift;

1→2). After a subsequent anneal in vacuum, the redshift is reversed (blue shift; 2→ 3). The insert, in Figure 3.5b, plots $(\alpha h\nu)^2$ versus $h\nu$ to demonstrate how IZO exhibits a Moss-Burstein shift [64], a decrease (or increase) in carrier concentration is caused by the increase (or decrease) of barrier height which in this cause is due to the excess oxygen adsorbed (or desorbed) in the IZO film during heat treatments in air (or vacuum). It is important to note that optical and electrical effects seen in these annealing experiments are macroscopic, and that changes seen α-IZO in this thesis are subtle at low temperatures and are likely due to minor rearrangements of the structure.

3.3 Convergence of Electrical Properties with Anneals

Annealing IZO films can change the electrical properties by several orders of magnitude. Leenheer [4] discovered that amorphous IZO films, once annealed, will converge towards a similar range of conductivities even if they were initially deposited with very different starting oxygen stoichiometries. IZO films of 60/40 to 84/16 at. percent In/Zn were sputtered with varying oxygen content (0-4%) in the sputter gas, as seen in Figure 3.7. The dotted line is a guide to the eye. As oxygen content in the sputter gas decreases, carrier concentration increases for all the films. The results indicate that differing compositions lay on the same line, meaning that mobility and carrier concentration exhibit a composition-independent behavior. When 70/30 at. percent In/Zn samples initially sputtered with varying oxygen content (0-4 percent) were annealed at 500 °C for one hour in both air and oxygen, the carrier concentration and mobility of the films converged to the same region. The carrier concentration N after the air anneal was $2.3\text{x}10^{19} \pm 0.8\text{x}10^{19}$ cm^{-3}, resulting in a mobility μ of 54 ± 1 cm^2/V s. After the oxygen anneal, N was $6.4\text{x}10^{18} \pm 2.0\text{x}10^{18}$ and μ was 45 ± 3 cm^2/V s. Note that the carrier concentration drops by a factor between 2 to 7 from the air anneal to the oxygen anneal, surprisingly close to the factor of 4.8 that would be expected because air is fractionally ~1/4.8 oxygen [4].

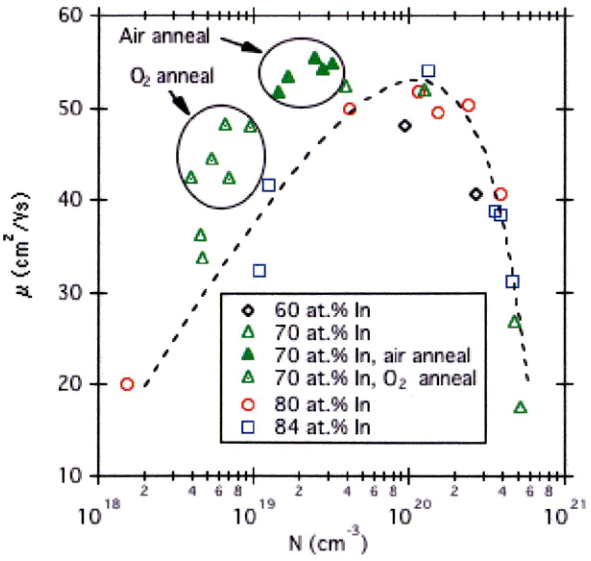

Figure 3.7 – Mobility as a funciton of carrier concentration for all films including 70 at. percent films annealed in air and oxygen.

Figure 3.7 confirms that the electrical properties of IZO are relatively independent of composition and strongly reliant on the oxygen content in sputter gas and annealing atmosphere. Work by Leenheer further supports the desorption of oxygen seen by Gonçalves et al. [56], and the importance of annealing atmosphere seen by Kim [59] and Major [58].

CHAPTER 4 – PRIMARY RESULTS

This text has been written for *Applied Physics Letters* and will be submitted once more analysis and some editing are finished.

4.1 Introduction

Transparent conducting oxides (TCOs) are used as transparent contacts in solar cells and displays, as electrochromic devices, and on glass as low-e windows [12-14, 29]. A recent focus in the TCO community is transparent thin film transistors (TTFTs). Amorphous indium zinc oxide (α-IZO) has shown promise as a candidate TCO for TTFT applications [8-10, 16]. Research on α-IZO TTFTs has recently identified an instability caused by persistent photoconductivity, which disrupts the on and off switching hysteresis of transistors [11]. Resistive IZO has also shown persistent instability upon heating (> 400 °C) resulting in an increase in conductivity by several orders of magnitude [58-60], but this temperature is outside the operating range for most TTFT applications.

In this paper, evidence is provided that highly resistive α-IZO films also demonstrate thermal instability even at temperatures as low as 120 °C, resulting in several orders of magnitude permanent increase in conductivity. Such large transitions in conductivity, especially at these lower temperatures, require consideration.

In this chapter, thermal instability is explored by electrical characterization accomplished by a four-point probe station with a heater. By varying the temperature from 170 to 120 °C the time of transition from a resistive to conductive state ranges from approximately two hours to three days. Such a dramatic evolution in conductivity has previously only been seen at higher temperatures, where crystallization and diffusional processes dominate. Several speculative models are offered to explain this low temperature time dependant instability.

IZO is amorphous in the composition range between 54-86 atomic percent In/Zn [2]. In this compositional range, heavy metal cations with electronic configurations of $(n-1)d^{10}ns^0$, where $n \geq 4$, are able to conduct electrons through non-directional spherically

symmetric *ns* orbitals because overlap still occurs even in their amorphous state [27, 28]. Electrical properties of indium zinc oxide are especially dependent on oxygen content and thus conductivity may be modified to serve as a conductive contact ($\sigma \sim 10^3$ S/cm), or a restive channel layer ($\sigma \sim 10^{-5}$ S/cm) [4, 65]. This configurability, combined with excellent transparency in the visible spectrum (>80 percent) [1], makes α-IZO extremely suitable for TTFT applications. As a further advantage, α-IZO may be deposited at room temperature via DC magnetron sputtering yielding a smooth, < 5nm roughness, uniform film suitable for flexible substrates [6, 7].

4.2 Experimental Setup

α-IZO thin films are produced on 5.08 x 5.08 cm Corning Eagle 2000 glass substrates using DC magnetron sputtering. Sputtering target to substrate distance is approximately 11 cm. The substrate glass is cleaned with Alconox, then rinsed with deionized water. 5.08 cm circular sputtering targets from Plasmaterials are used with a composition of 84/16 atomic percent In/Zn. The sputtering chamber is pumped down to a pressure < $5x10^{-6}$ torr. A ratio of 90/10 percent argon to O_2 is employed with a sputter pressure of 4.5 mtorr in the chamber at a 40 W power setting, or 2 W/cm^2 normalized. Samples are deposited with 10 percent O_2 to produce a highly resistive beginning state, $\sigma \sim 10^{-4}$ S/cm. A burn-in time of ten minutes is applied to rid the target surface of contaminants and to equalize the target with the sputter gas.

Film thickness is determined by a Cauchy dispersion relation to fit ellipsometic data measured by an α–SE Woollam Company spectroscopic ellipsometer. All films deposited are ~250 nm ± 20 nm thick. Optical transmittance and reflectance spectra are measured by a multi-channel fiber-optically-coupled CCD-array-based spectrometer (Ocean Optics). Film thickness is verified by optical measurements in combination with optical modeling. Evaporated Ti/Au electrodes on the IZO film serve as contact pads for a four-point probe measurement system with an integrated ceramic substrate heater. The contact pads are 3.6 mm by 0.83 mm. They are spaced in doublet-sets separated 1.68 mm, with a spacing difference of 0.67 mm between sets. Reported conductivities are not corrected for the contact geometry, and therefore represent relative, rather than absolute

values. Temperature is measured and controlled on the front surface of the film using a Eurotherm 2416 controller. Samples reach the desired temperature in approximately 40 seconds. All samples were annealed in atmosphere.

4.3 Results

Figure 4.1 illustrates the effect of heating on the conductivity of α-IZO films as a function of time at several temperatures between 120-170 °C. These isothermal profiles indicate that the transition to high conductivity occurs more rapidly at higher temperatures. The conductive state is ~5-6 orders of magnitude more conductive than the resistive state in these heat-treated films. It appears that the film conductivity approaches a saturation at long times, although this saturation behavior was not fully captured in these scans. At the beginning of each temperature scan (~10 seconds) there is a rapid jump in the conductivity by nearly an order of magnitude. This abrupt initial jump is attributed to reversible temperature dependent conductivity. Electrical conductivity is

$$\sigma = e\mu N$$

Equation 4.1

where conductivity is σ (S/cm), e is the charge on a carrier, μ is the mobility of the carriers, and N is the carrier concentration. The initial reversible temperature dependence of σ comes from N, which is exponentially dependent on temperature due to

$$N = N_o e^{\frac{-En}{k_b T}}$$

Equation 4.2

where N_o is a prefactor, E_n is the activation energy for carriers, and k_b is the Boltzmann constant. This initial reversible conductivity increase is distinct from the slower, irreversible conductivity increase caused by the heat treatment. The jump in conductivity at the end of the 160 °C profile is attributed to too much current forced through the sample, causing further local heating.

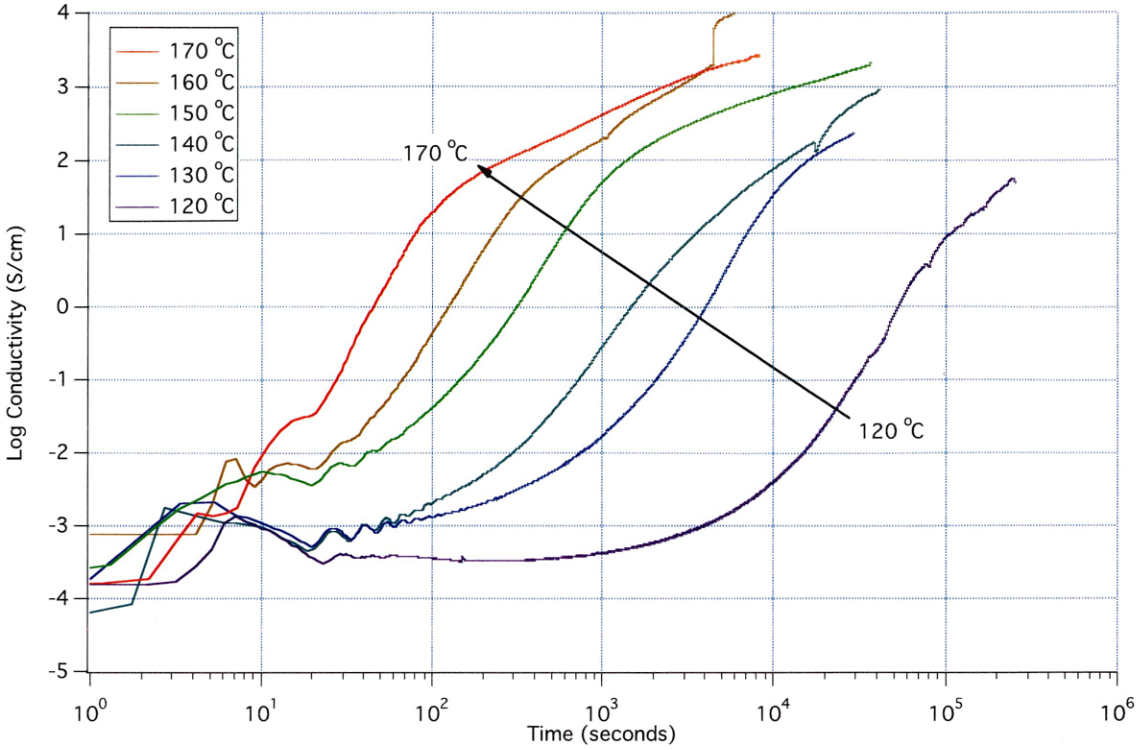

Figure 4.1 – Time dependence of thermally activated electrical conductivity in α-IZO.

The XRD data presented in Figure 4.2 indicates that there is no appreciable change in the amorphous peak before or after the temperature scans. However, there is evolution of a small peak at ~30 degrees superimposed on the diffuse amorphous background, which might be attributed to relaxation of the amorphous IZO phase. Relaxation could allow realignment of bonds to a more locally ordered state, which is indicated by the appearance of the new peak. However, it is important to note that 120, 140 and 160 °C data did not evolve the peak at approximately thirty degrees; suggesting that the peak is not essential to the conductivity change. Also, the peak does not seem to appear at the same angle suggesting it could be an artifact.

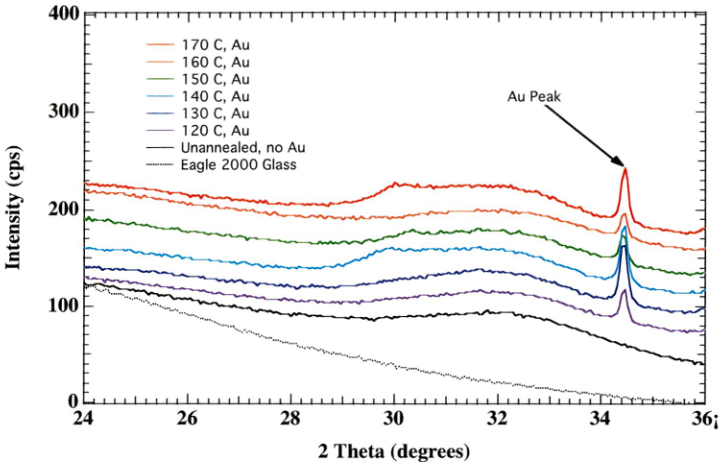

Figure 4.2 – XRD scans of 120-170 °C temperature samples offset. The peak at 34.5 degrees is the gold peak of the contacts on the samples. There is an appearance of an amorphous peak ~30 degrees in 170, 150, and 140 data.

Figure 4.3 presents transmission and reflection of a representative heat-treated (130 °C) α-IZO sample and a non-heated reference. Transmission and reflection data indicate that all films are transparent, > 80 percent, before and after annealing for all annealing temperatures. The difference in the two curves is mostly due to thickness differences of the two samples.

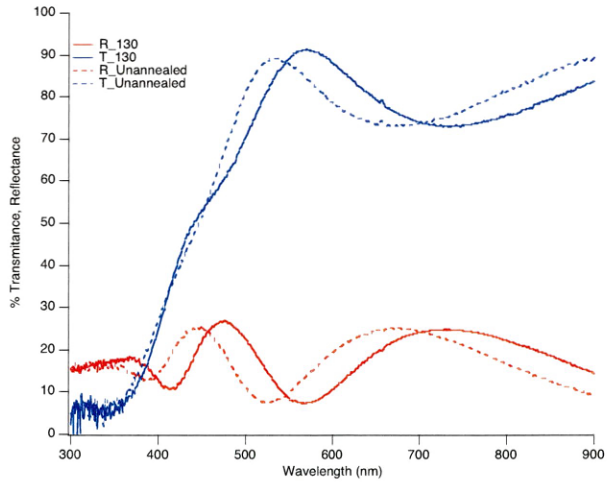

Figure 4.3 – Reflection and transmission of the 130 °C anneal and its reference thin film.

4.4 Discussion

The newly observed thermally activated electrical conductivity effect seen between 120-170 °C in highly resistive α-IZO has previously been reported only at temperatures > 400 °C [58-60]. To demonstrate that this process is activated, figure 4.4 shows an inflection point analysis of the isothermal conductivity profiles on an Arrhenius plot, providing an activation energy of approximately 2.04 eV. In previous temperature investigations, heating above 400 °C triggered a structural transition from amorphous to crystalline IZO, and the observed increases in conductivity were attributed to this structural transition. As the XRD data in Figure 4.2, demonstrates, however, no detectable or large-scale crystallization takes place in these lower temperature heat treatments. Nevertheless, these previous studies underscore the propensity of resistive IZO to become more conductive upon heating. In amorphous indium oxides, α-In_2O_3, conductivity is also seen to increase by orders of magnitude upon heating at relatively low temperatures (150-180 °C) [62]. Here again, however, the increase in conductivity occurs in concert with a transition from the amorphous to the crystalline phase. The fact that this thermally activated electrical conductivity effect is seen in both α-IZO and α-In_2O_3 suggests that similar mechanisms are at work [25]. Persistent photoconductivity in α-In_2O_3 has been shown to alter conductivity in much the same way as α-IZO [62, 63], increasing the correlations between the two materials.

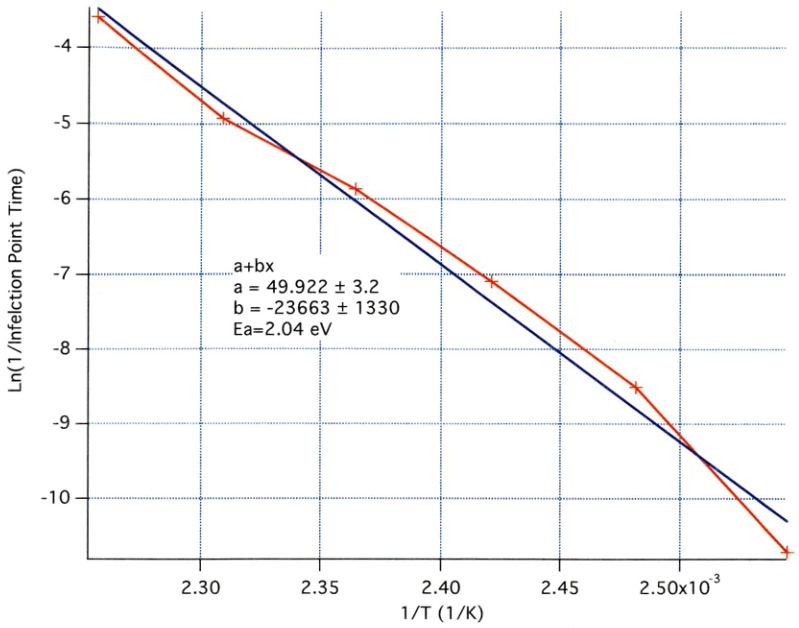

Figure 4.4 – Natural log of the inflection point time for each isothermal scan as a function of inverse temperature.

Previous IZO and α-In_2O_3 studies have attributed conductivity changes to an oxygen diffusion process, assisted either thermally or optically [58-60, 62, 63]. Oxygen stoichiometry is important to many TCO properties because ideal oxygen vacancies delocalize or donate two electrons, as seen in figure 4.5, increasing charge carrier concentration, as seen in equation 4.3 in Kröger-Vink notation.

$$O_o^x \Leftrightarrow \frac{1}{2}O_{2(g)} + V_o^{\bullet\bullet} + 2e'$$

Equation 4.3

It must be understood that construct of Kröger-Vink notation is used as a physical representation of electronic properties in crystalline solids. IZO in this study is amorphous, and strictly speaking does not have lattice sites and actual oxygen vacancies. However, dangling bonds still exist, and from a viewpoint of electronic structure are functionally similar to oxygen vacancies.

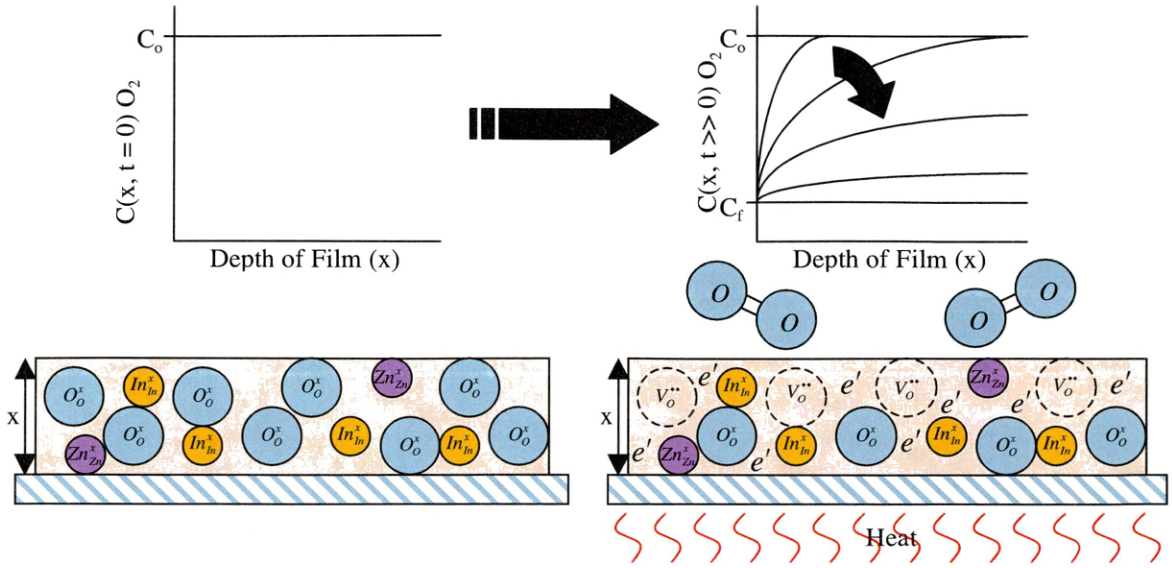

Figure 4.5 – A representation of an IZO film on glass with the concentration of oxygen decreasing when heat is applied.

The oxygen diffusion effect has been shown to be thermally reversible in crystalline IZO by heating to high temperatures in either oxygen atmosphere (to reduce carrier concentration), or in vacuum (to increase carrier concentration) [58-60, 62]. This effect is not seen when α-IZO is annealed at 150 °C under vacuum. Table 4.1 shows before and after results of similar samples annealed in oxygen, air, and under vacuum. Films annealed in oxygen, air, and vacuum all produced more conductive films than the original resistive state ($\Delta\sigma > 10^5$). Even samples that were first annealed in vacuum and air did not transition back to a resistive state when subsequently annealed in oxygen; they actually continued to increase in conductivity. The distinguishing feature of previous literature results (where the oxygen environment during annealing is observed to strongly affect film conductivity) and the results presented in Table 4.1 (where the oxygen environment during annealing does not affect film conductivity) is that much lower temperatures were explored in this study. These observations suggest that diffusion is not the mechanism that drives the low temperature (120-170 °C) permanent conductivity increase in these resistive α-IZO films. Instead, this data indicates the process is not reversible and mostly dependent on time and temperature, both of which could connect to diffusion of oxygen but do not.

Table 4.1 – α-IZO anneals under various partial pressures of O_2.

		IZO Anneal at 150 °C for 16 hours		Additional Anneal at 150 °C for 16 hours	
Sample	Beginning Conductivity (S/cm)	Partial Pressure O_2 (atm)	Conductivity (S/cm)	Partial Pressure O_2 (atm)	Conductivity (S/cm)
1	3.03E-06	0.21 atm	103	6E-6 atm	214
2	3.03E-06	6E-6 atm	3.61	6E-6 atm	--
3	3.03E-06	1E-10 atm	0.389	6E-6 atm	47.6

As further evidence that the observed conductivity changes cannot likely be explained by oxygen diffusion effects, diffusion-based models do not appear to provide a satisfactory fit to the observed film behavior. For example, one way to model the thermally activated conductivity behavior is to correlate the time-dependence of the conductivity increase to a simple one-dimensional transient diffusion process of oxygen out of the film. This model assumes that the observed time-dependent conductivity increase can be attributed wholly to increases in carrier concentration due to diffusion of oxygen out of the film. Based on this assumption, the long-time approximation to Fick's second law for finite one-dimensional transient diffusion yields the following conductivity versus time dependence:

$$\sigma(t) \propto \sigma_f + (\sigma_o - \sigma_f)e^{\frac{-Dt}{L^2}}$$

Equation 4.4

where σ_o is initial conductivity, σ_f is final conductivity, t is time, L is the film thickness, and D, the diffusivity, is exponentially dependent on temperature:

$$D = D_o e^{-\frac{E_D}{k_b T}}$$

Equation 4.5

where D_o is the pre-exponential factor, and E_D is the diffusion activation energy. Figure 4.6 represents the fit of this diffusion model to the experimental data. D is the only parameter that is fit in this equation, and D depends on E_D, which provides little flexibility while fitting. The fit does not conform to the data, as the diffusion model predicts a much slower rate of transition from the resistive to conductive states than is

experimentally observed. This finding provides further evidence that oxygen diffusion does not govern the conductivity changes occurring in α-IZO at low temperatures.

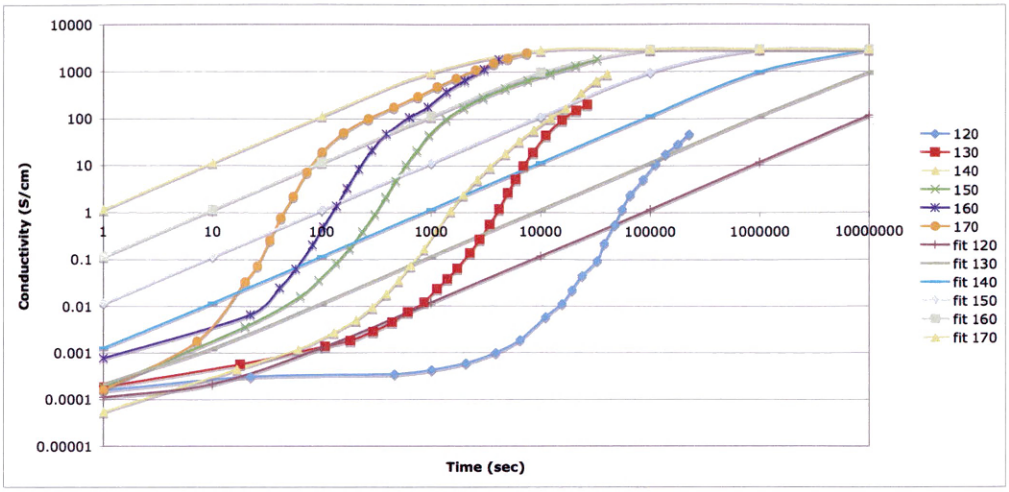

Figure 4.6 – Plot of temperature profiles of conductivity with respect to time with diffusion model fit.

Although the observed thermally activated conductivity transition cannot be modeled using a one-dimensional diffusion process, the sigmoidal behavior is characteristic of a nucleation and growth process. In this sample, no crystallization is seen but XRD scans hint at a possible relaxation of the amorphous phase. The Avrami-Johnson-Mehl model [66-68], describes the transition from amorphous to crystalline phases through solid-state phase transformation by nucleation and growth. This model provides the crystalline fraction of material transformed as a function of time:

$$\chi(t) = 1 - e^{-\left(\frac{t-\tau_o}{\tau_r}\right)^n}$$

Equation 4.6

where t is the time, τ_o is the onset time before relaxation of the amorphous phase, τ_r is the characteristic relaxation time of the amorphous phase, and n, the Avrami-Johnson-Mehl exponent, ranges from 1-4 depending on the dimensionality of the nucleation and growth process. An Avrami-Johnson-Mehl exponent $1<n<2$ is associated with one-dimensional nucleation and growth, while $2<n<3$ is associated with two-dimensional nucleation and growth, and $3<n<4$ is associated with three-dimensional nucleation and growth. In the

context of the present study, the Avrami-Johnson-Mehl model is used to describe the time-dependent transformation of the IZO film from the initially resistive state to the final conductive state. In previous work on amorphous silicon [66, 68], τ_o was the incubation time before crystallization began and τ_r was the characteristic crystallization time. The terminology change from crystallization to relaxation is necessary to emphasize that crystallization does not occur. The conductivity transition is perhaps associated with amorphous relaxation, as seen in the appearance of the amorphous IZO XRD peak in Figure 4.2. This relaxation may proceed by a pseudo-nucleation and growth process, as the initially uniformly resistive film transforms to a bond realigned, highly conducting film. Assuming that the film conductivity is directly proportional to the transformed fraction of material yields the following equation:

$$\sigma(t) \propto \sigma_f + (\sigma_o - \sigma_f) e^{-\left(\frac{t-\tau_o}{\tau_r}\right)^n}$$

Equation 4.7

Where τ_o, τ_r, and n are used as fitting parameters for the Avrami-Johnson-Mehl equation. Paine et al. [67] used the same model to relate the change in resistivity of tin doped indium oxide (ITO) to relaxation of amorphous to crystalline phases. However, this work does not ever measure relaxed amorphous fraction; rather, the Avrami-Johnson-Mehl model is assumed to represents a refinement where some percolation mechanism, not considered in this current model, has a linearly proportionality to the amount relaxed amorphous structure. Figure 4.7 illustrates that the model nicely fits the experimental data at intermediate times with $n = 3.5$, indicating a three-dimensional transformation process. Even though the model is not representative of a perfect physical process, the fit is good and does not change the results seen in the experiment. The activation energy associated with relaxation of the amorphous structure was determined in the usual way from an Arrhenius plot in which the logarithm of the onset time and characteristic relaxation time as a function of inverse temperature. An Arrhenius plot of τ_o, provided in figure 4.8, and τ_r, provided in figure 4.9, indicates a rate-activated process with E_a approximately1.82 eV and 1.99 eV, respectively. In amorphous silicon [66], activation energy range from 2.7 eV for τ_o and 3.9 eV for τ_r. In ITO [67], activation energies were approximately 1.3 ± 0.2 eV. IZO activation energies are relevant since they fall right

between amorphous silicon and ITO. In comparison, the inflection point analysis of activation energy, in figure 4.3, provides approximately 2.04 eV and is fairly close to activation energies of τ_o and τ_r for IZO.

4.5 Summary

Heating resistive samples of α-IZO at temperatures of 120-170 ^{o}C has lead to the discovery of a thermally activated, time-dependant, permanent transition in electronic conductivity, from ~10^{-4} to ~10^{3} S/cm. Although the annealed α-IZO samples do not crystallize, XRD spectra of the annealed films do show a small appearance in the amorphous peak, which could be consistent with minor structural reordering in the films. One possibility is that this structural reordering may free electrons for transport by reordering oxygen bonds, thereby leading to the increased conductivity. Based on experimental and model analysis, oxygen diffusion was dismissed as a possible model for the observed conductivity changes. As a speculative alternate explanation, an Avrami-Johnson-Mehl model was presented to relate the observed thermally activated electronic conductivity effect to amorphous structural relaxation. Further research on α-IZO must be accomplished to appreciate the basic material science behind this mechanism before quality stable TTFT devices are possible.

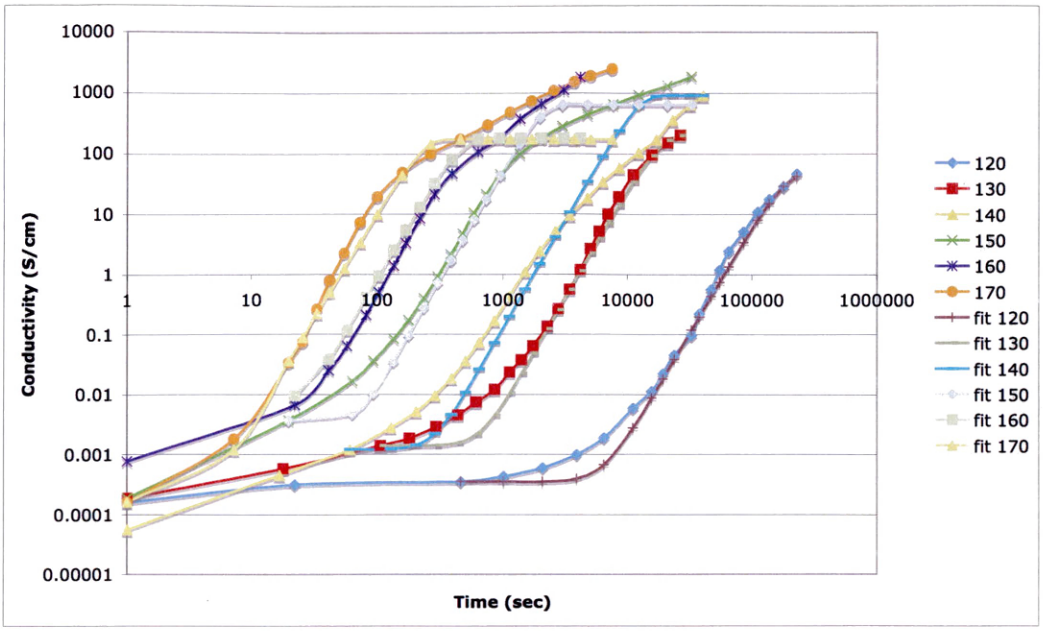

Figure 4.7 – Plot of temperature profiles of conductivity with respect to time with Avrami-Johnson-Mehl model fit.

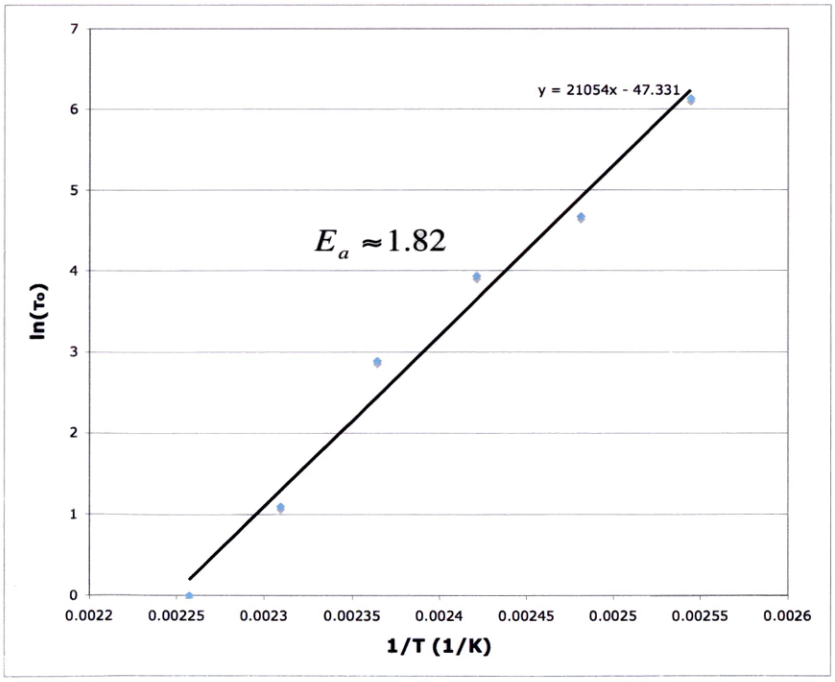

Figure 4.8 – Arrhenius plot of onset time τ_o as a function of inverse temperature. The slope provides the activation energy.

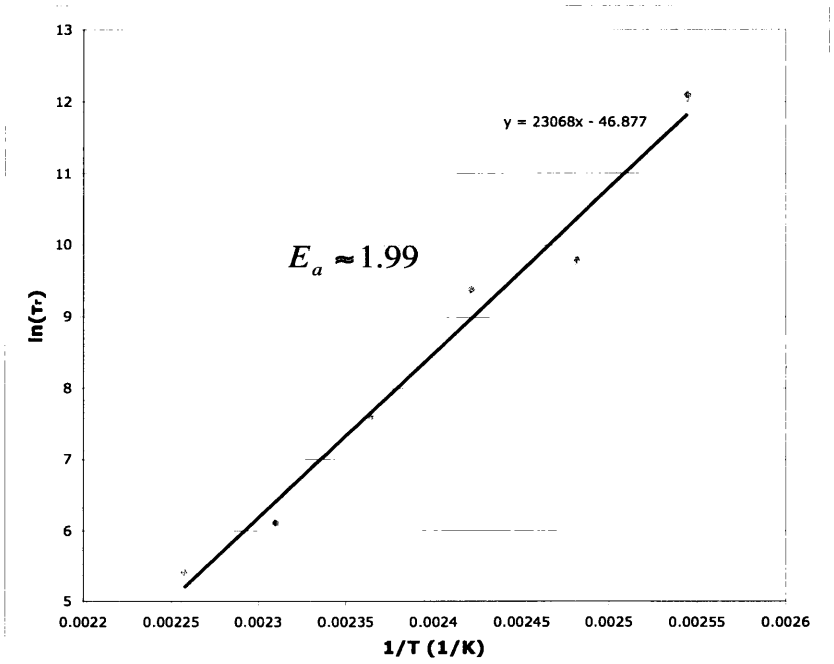

Figure 4.9 – Arrhenius plot of onset time τ_r as a function of inverse temperature. The slope provides the activation energy.

CHAPTER 5 – ADDITIONAL RESULTS

5.1 TPD on α-IZO

Temperature programmed desorption was used to test if there were any gaseous species coming from α-IZO when heated that might explain the extreme increase in conductivity. Removing α-IZO from the glass is extremely difficult; therefore, Kapton tape had to be used to remove the thin film from the glass substrate after deposition. This sample was grown on Kapton tape covered Corning Eagle 2000 glass under the same deposition parameters as other films. Films were grown for a longer time to create more material to improve the TPD signal.

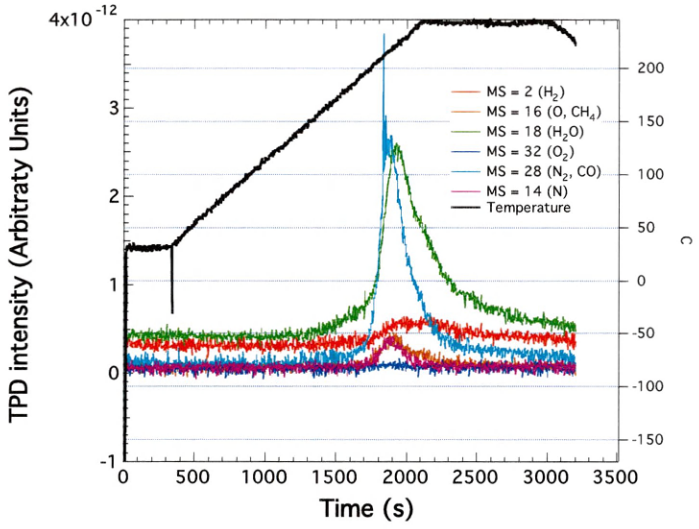

Figure 5.1 – TPD of α-IZO. Large amounts of H_2O, at an AMU of 18, and N_2 or CO, at an AMU of 28, were detected.

Approximately 3mg of α-IZO was used in this TPD experiment. After the sample was placed in the test tube, it was heated to 100 °C to desorb any contaminates from the film surface, such as water. After cooling, the sample was reheated to 25 °C, after which a slow temperature ramp to 250 °C was induced. Figure 5.1 shows the TPD data as a function of time, which indicates no appreciable amount of O_2 molecules, dark blue curve, were detected. Figure 5.2 is a 200 °C temperature slice of the molecules

detected by the quadrupole mass spectrometer (QMS). The interesting peak in Figure 5.2 is the peak at 30 AMU. It seems that there might be a large contamination of Kapton molecules or carbon itself might have absorbed to the instrument from previous experiments. The nano-carbon group at NREL uses the TPD a lot. Therefore, one possibility could be oxygen radicals desorbing from the film and then interacting with carbon or other molecules before passing though the QMS. This certainly could be the case seen in peaks at 28 AMU, carbon monoxide, and 44 AMU, carbon dioxide.

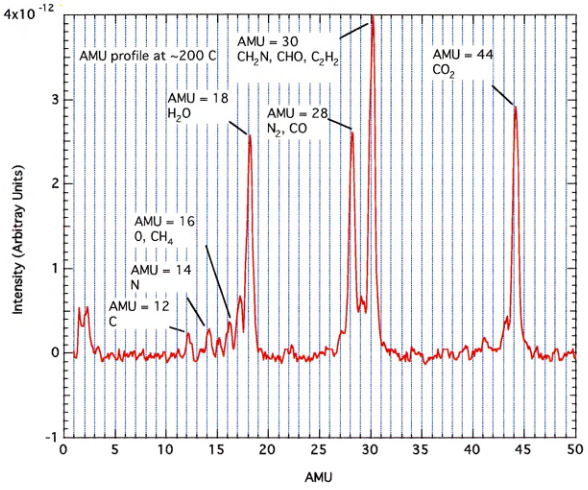

Figure 5.2 – 200 °C temperature slice of TPD experiment showing species detected in the RGA.

At first, the data suggests oxygen is not desorbing from the film, but this is only one TPD experiment. There could be sufficient contamination from either the Kapton tape or from the measurement instrument. Also, the QMS used in this TPD experiment might not be able to detect such low levels of oxygen. Theoretically, α-IZO requires less than one percent of the oxygen to desorb in the film to see large changes in conductivity. This small amount of oxygen is actually close to the detectablity limit of the QMS unit. In any case, further studies in TPD might be able to reveal if any oxygen or other species is desorbing from the film. However, at this point results are inconclusive.

CHAPTER 6 – CONCLUSIONS AND FUTURE WORK

6.1 Conclusions

Thermally activated, time-dependant, permanent electronic conductivity in α-IZO thin films was quantified by using a ceramic heater in conjunction with a four-point probe. The conductivity changed by nearly seven orders of magnitude, from $\sim 10^{-4}$ to $\sim 10^{3}$ S/cm, as long as samples were given enough time to reach an equilibrium state at temperatures ranging from 120 to 170 °C. The films before and after heating were >80 percent optically transparent in the visible spectrum. XRD scans of the temperature profiles indicate the appearance of an amorphous peak in the α-IZO, which suggests a mild relaxation of the amorphous structure. The models explored in order to explain the occurrence of thermally activated, time-dependant, permanent electronic conductivity eliminated diffusion as a possibility; however, a speculative rudimentary Avrami-Johnson-Mehl model links structural relaxation to the increase in conductivity.

6.2 Future Work

Further studies on annealing effects on indium zinc oxide will advance the understanding of this TCO system. While low temperature annealing caused the conductivity to change several orders of magnitude, the mechanisms behind this change are not well understood and current models are not sufficient to explain the results, other than to rule out diffusion. Therefore, more annealing tests and characterization are required.

In this study only one composition regime (84/16 at. percent In/Zn) was utilized for annealing. IZO is amorphous between 54 and 85 at. Percent In/Zn. Also, only 10 percent O_2 in the argon sputtering gas was used during the sputtering process. An examination of both the In/Zn ratio and percent oxygen in the sputter gas should follow up. This inspection would provide further insight into which species dominate the annealing/conductivity effect seen during this study. In particular, the amount of oxygen present in the film is known to affect the electrical properties. However, it is not known

how the oxygen content or composition ratio affects the rate of reaction or the end annealing result. A more complete data set of IZO annealing studies would provide the insight necessary to fit models. Testing other amorphous TCOs for low temperature activated increase in electrical conductivity could provide further insight into the nature of this extraordinary change and if it is unique to α-IZO. Also, temperature dependent hall probe measurements could help to ascertain the conduction mechanism of the thermally activated, time-dependant, permanent electronic conductivity effect.

The initial work motivation in this study was on persistent photoconductivity of IZO films. By exposing IZO film samples to ultraviolet light, conductivity is observed to increase by 1-2 orders of magnitude. Photoconductivity experiments ceased upon discovering the annealing affect on conductivity; it was a more fundamental change to the sample. However, reexamining photoconductivity coupled with annealing might help determine the mechanisms of the changing conductivity.

Amorphous film structure is difficult to determine because of its short range order. The knowledge of amorphous structure is mired in the details of normal characterization techniques, such as XRD. However, more powerful techniques can be employed to further probe the structure and the rearrangement taking place, like solid state nuclear magnetic resonance spectroscopy or synchrotron characterization.

Since IZO has shown sensitivity to oxygen, temperature, and light, it could be utilized to produce sensors of each type. Oxygen sensors are numerous; however, IZO could be exploited in intermediate temperature applications (500-600 °C) where it has been shown to absorb and desorb oxygen. As a temperature sensor, IZO could function as a one-time use sensor, such as a fuse. IZO could be used in applications ranging from photolithography to sun tanning industries since IZO is sensitive to ultraviolet light. IZO, as a TCO, has an inherent advantage over other sensors being transparent and still able to relay sensing information electronically.

REFERENCES CITED

[1] Y. S. Jung, J. Y. Seo, D. W. Lee, and D. Y. Jeon, "Influence of DC magnetron sputtering parameters on the properties of amorphous indium zinc oxide thin film," *Thin Solid Films,* vol. 445, pp. 63-71, 2003.

[2] M. P. Taylor, "Indium Zinc Oxide Thin Films: A Novel Family of Transparent Conducting Oxides," in *Materials Science*. vol. Ph.D. Golden, Colorado: Colorado School of Mines, 2005, p. 196.

[3] E. Fortunato, A. Pimentel, A. Gonçalves, A. Marques, and R. Martins, "High mobility amorphous/nanocrystalline indium zinc oxide deposited at room temperature," *Thin Solid Films,* vol. 502, pp. 104-107, 2006.

[4] A. Leenheer, "Control of Electron Transport in Sputtered Amorphous Transparent Indium Zinc Oxide Thin Films," in *Material Science* Masters, Golden: Colorado School of Mines, 2007, p. 74.

[5] Y. S. Song, J. K. Park, T. W. Kim, and C. W. Chung, "Influence of process parameters on the characteristics of indium zinc oxide thin films deposited by DC magnetron sputtering," *Thin solid Films,* vol. 467, pp. 117-120, 2004.

[6] N. Ito, Y. Sato, P. K. Song, A. Kaijio, K. Inoue, and Y. Shigesato, "Electrical and optical properties of amorphous indium zinc oxide films," *Thin Solid Films,* vol. 496, pp. 99-103, 2005.

[7] Sasabayashi T., N. Ito, K. M., P. K. Song, Ustumi K., A. Kaijio, and Y. Shigesato, "Comparative study on structure and internal stress in tin-doped indium oxide and indium-zinc oxide films deposited by r.f. magnetron sputtering," *Thin Solid Films,* vol. 445, pp. 219-223, 2003.

[8] P. Barquinha, A. Pimentel, A. Marques, L. Pereira, R. Martins, and E. Fortunato, "Influence of the semiconductor thickness on the electrical properties of transparent TFTs based on indium zinc oxide," *Journal of Non-Crystalline Solids,* vol. 352, pp. 1749-1752, 2006.

[9] N. L. Dehuff, E. S. Kettenring, D. Hong, H. Q. Chiang, J. F. Wager, R. L. Hoffman, C.-H. Park, and D. A. Keszler, "Transparent thin-film transistors with zinc indium oxide channel layer," *Journal of Applied Physics,* vol. 97, p. 064505, 2005.

[10] B. Yaglioglu, H. Y. Yeom, R. Beresford, and D. C. Paine, "High mobility amorphous In_2O_3-10wt%ZnO thin film transistors," *Applied Physics Letters,* vol. 89, p. 062103, 2006.

[11] P. Barquinha, A. Pimentel, A. Marques, L. Pereira, R. Martins, and E. Fortunato, "Effect of UV and visible light radiation on the electrical performances of transparent TFTs based on amorphous indium zinc oxide," *Journal of Non-Crystalline Solids,* vol. 352, pp. 1756-1760, 2006.

[12] R. G. Gordon, "Criteria for Choosing Transparent Conductors," *MRS Bulletin,* vol. 25, pp. 52-57, August 2000.

[13] B. G. Lewis and D. C. Paine, "Applications and Processing of Transparent Conducting Oxides," *MRS Bulletin,* vol. 25, pp. 22-27, August 2000.

[14] E. Fortunato, D. S. Ginley, H. Hosono, and D. C. Paine, "Trasparent Conducting Oxides for Photovoltaics," *MRS Bulletin,* vol. 32, pp. 242-247, 2007.

[15] D. S. Ginley and C. Bright, "Transparent Conducting Oxides," *MRS Bulletin,* vol. 25, pp. 15-18, August 2000.

[16] K. Nomura, H. Ohta, A. Takagi, T. Kamiya, M. Hirano, and H. Hosono, "Room-temperature fabrication of transparent flexible thin-film transistors using amorphous oxide semiconductors," *Nature,* vol. 432, pp. 488-492, 2004.

[17] K. Badeker, "Ueber die elektrische Leitfahigkeit und die thermoelektrische Kraft einiger " *Analytical Physics (Leipzig),* vol. 22, pp. 749-766, 1907.

[18] H. L. Hartnagel, A. L. Dawar, A. K. Jain, and C. Jagadish, *Semiconducting Transparent Thin Films*. Bristol: Institute of Physics Publishing, 1995.

[19] G. Haacke, "Transparent Conducting Coatings," *Annual Review Material Science,* vol. 7, pp. 73-93, 1977.

[20] H. Kawazoe, H. Yanagi, K. Ueda, and H. Hosono, "Transparent p-Type Conducting Oxides: Design and Fabrication of *p-n* Heterojunctions," *MRS Bulletin,* vol. 25, pp. 28-36, 2000.

[21] M. F. A. M. van Hest, M. S. Dabney, J. D. Perkins, D. S. Ginley, and M. P. Taylor, "Titanium-doped indium oxide: A high-mobility transparent conductor," *Applied Physics Letters,* vol. 87, p. 032111, 2005.

[22] C. Warmsingh, Y. Yoshida, D. W. Readey, C. W. Teplin, J. D. Perkins, P. A. Parilla, L. M. Gedvilas, B. M. Keyes, and D. S. Ginley, "High-mobility transparent conducting Mo-doped In_2O_3 thin films by pulsed laser deposition," *Journal of Applied Physics,* vol. 95, pp. 3831-3833, April 1, 2004 2004.

[23] T. Moriga, D. D. Edwards, T. O. Mason, G. B. Palmer, K. R. Poeppelmeier, J. L. Schindler, C. R. Kannewurf, and I. Nakabayashi, "Phase Relationships and Physical Properties of Homologous Compounds in the Zinc Oxide-Indium Oxide System," *Journal of the American Ceramic Society,* vol. 81, pp. 1310-1316, 1998.

[24] M. P. Taylor, D. W. Readey, C. W. Teplin, M. F. A. M. van Hest, J. L. Alleman, B. M. Keyes, B. To, P. A. Parilla, J. D. Perkins, and D. S. Ginley, "Combinatorial Growth and Analysis of the Transparent Conducting Oxide ZnO/In (IZO)," *Macromolecular Rapid Communications,* vol. 25, pp. 344-347, 2004.

[25] B. Yaglioglu, Y.-J. Huang, H.-Y. Yeom, and D. C. Paine, "A study of amorphous and crystalline phases in In_2O_3-10 wt.% ZnO thin films deposited by DC magnetron sputtering," *Thin Solid Films,* vol. 496, pp. 89-94, 2006.

[26] H. Hosono, M. Yasukawa, and H. Kawazoe, "Novel oxide amorphous semiconductors: transparent conducting amorphous oxides," *Journal of Non-Crystalline Solids,* vol. 203, pp. 334-344, 1996.

[27] H. Hosono, N. Kikuchi, N. Ueda, and H. Kawazoe, "Working hypothesis to explore novel wide band gap electrically conducting amorphous oxides and examples," *Journal of Non-Crystalline Solids,* vol. 198-200, pp. 165-169, 1996.

[28] H. Hosono, "Ionic amorphous oxide semiconductors: Material design, carrier transport, and device application," *Journal of Non-Crystalline Solids,* vol. 352, pp. 851-858, 2006.

[29] T. J. Coutts, D. L. Young, and X. Li, "Characterization of Transparent Conducting Oxides," *MRS Bulletin,* vol. 25, pp. 58-65, August 2000.

[30] F. A. Kröger, *Chemistry of Imperfect Crystals.* Amsterdam: North-Holland, 1964.

[31] M. P. Taylor, D. W. Readey, C. W. Teplin, M. F. A. M. van Hest, J. L. Alleman, M. S. Dabney, L. M. Gedvilas, B. M. Keyes, B. To, J. D. Perkins, and D. S. Ginley, "The electrical, optical and structural properties of $In_xZn_{1-x}O_y$ ($0 \leq x \leq 1$) thin films by combinatorial techniques," *Measurement Science and Technology,* vol. 16, pp. 90-94, 2005.

[32] D. Y. Ku, I. H. Kim, I. Lee, K. S. Lee, T. S. Lee, J.-h. Jeong, B. Cheong, Y.-J. Baik, and W. M. Kim, "Structural and electrical properties of sputtered indium-zinc oxide thin films," *Thin Solid Films,* vol. 515, pp. 1364-1369, 2006.

[33] M. H. Cohen, H. Fritzsche, and S. R. Ovshinsky, "Simple Band Model for Amorphous semiconducting Alloys," *Physical Review Letters,* vol. 22, p. 1065, 1969.

[34] S. N. Mott, "Electrons in Glass," *Reviews of Modern Physics,* vol. 50, p. 203, 1978.

[35] D. Adler, B. B. Schwartz, and M. C. Steele, *Physical Properties of Amorphous Materials*. New York: Plenum Press, 1985.

[36] C. Kittel, *Introduction to Solid State Physics*, 8th ed. ed. New York: John Wiley & Sons, 2005.

[37] D. M. Mattox, *The Foundations of Vacuum Coating Technology*. Norwich, NY: Noyes/William Andrew Publishing, 2003.

[38] *PVD Coatings - Your guide to PVD coating technology, applications and theory*. www.pvd-coatings.co.uk, online source accessed on October 16th, 2007.

[39] B. Chapman, *Glow Discharge Processes*. New York: John Wiley & Sons, 1980.

[40] A. R. Stephen T. Thornton, *Modern Physics for Scientists and Engineers*, 2nd ed. Jefferson City, MO: Thompson Learnig, Inc., 2002.

[41] D. L. Young, "Electron Transport in Zinc Stannate (Zn_2SnO_4) Thin-Films," in *Applied Physics*. vol. Ph.D. Golden, Colorado: Colorado School of Mines, 2000, p. 218.

[42] L. B. Valdes, "Resistivity Measurements on Germanium for Transistors," *Proceedings of the IRE,* vol. 42, pp. 420-427, February 1954.

[43] J. Clark, *Four Point Probe Theory*. http://www.four-point-probes.com/, Online source accessed August 2007.

[44] J. Clark, *Notes on Four Point Resistivity Measuring With Jandel Equipment*. http://www.four-point-probes.com/, Online source accessed August 2007.

[45] F. M. Smits, "Measurement of Sheet Resistivities with the Four-Point Probe," *The Bell System Technical Journal,* pp. 711-716, October 15 1957.

[46] D. K. Schroder, *Semiconductor Material and Device Characterization*. New York: John Wiley & Sons, Inc., 1990.

[47] U. Rossow, "The early history of ellipsometry," in *4th International Conference on Spectroscopic Ellipsometry*, Stocjholm, Sweden, 2007.

[48] H. Fujiwara, *Spectroscopic Ellipsometry: Principles and Applications*. New York: John Wiley and Sons, Ltd., 2007.

[49] J. A. Wollam, "Version 2.03 alpha-SE Software Manual."

[50] J. I. Pankove, *Optical Processes in Semiconductors*. New York: Dover Publications, Inc., 1971.

[51] B. D. Cullity and S. R. Stock, *Elements of X-Ray Diffraction*, 3rd ed. Upper Saddle River, NJ: Prentice Hall, 2001.

[52] S. O. Kasap, *Principles of Electronic Materials and Devices*, 2nd ed. ed. New York: McGraw-Hill, 2002.

[53] J. A. W. Elliot and C. A. Ward, "Temperature programmed desorption: A statistical rate theory," *Journal of Chemical Physics,* vol. 106, pp. 5677-5684, 1997.

[54] R. M. Nix, *An Introduction to Surface Chemistry.* http://www.chem.qmul.ac.uk/surfaces/scc/, 2003.

[55] B. Yaglioglu, H. Yeom, and D. C. Paine, "Crystallization of amorphous In2O3-10wt% ZnO thin films annealed in air," *Applied Physics Letters,* vol. 86, p. 261908, 2005.

[56] A. Gonçalves, P. Barquinha, L. Raniero, R. Martins, and E. Fortunato, "Crystallization of amorphous indium zinc oxide thin films produced by radio-frequency magnetron sputtering," *Thin Solid Films,* 2007.

[57] M. P. Taylor, D. W. Readey, M. F. A. M. van Hest, C. W. Teplin, J. L. Alleman, M. S. Dabney, L. M. Gedvilas, B. M. Keyes, B. To, P. A. Parilla, J. D. Perkins, and D. S. Ginley, "The Remarkable Thermal Stability of Multi-Cation Amorphous Transparent Conductors," *Nature Materials,* p. Submitted for publication 2007.

[58] S. Major, A. Banerjee, and K. L. Chopra, "Annealing studies of undoped and indium-doped films of zinc oxide," *Thin Solid Films,* vol. 122, pp. 31-43, 1984.

[59] H.-W. Kim, J.-S. Ahn, and K.-C. Je, "Reversible Electrical and Optical Behaviors due to Excess Oxygen in RF-Sputtered In_2O_3-ZnO Films," *Japan Journal of Applied Physics,* vol. 42, pp. 5714-5717, 2003.

[60] P. Barquinha, A. Gonçalves, L. Pereira, R. Martins, and E. Fortunato, "Effect of annealing temperature on the properties of IZO films and IZO based transparent TFTs," *Thin Solid Films,* 2007.

[61] F. A. Kröger, *Chemistry of Imperfect Crystals*. Amsterdam: North-Holland, 1974.

[62] B. Pashmakov, B. Claflin, and H. Fritzsche, "Transport Near the Mobility Edge, the Sign of the Hall Effect, Photoreduction and Oxidation of Amorphous InOx," *Journal of Non-Crystalline Solids,* vol. 164-166, pp. 441-444, 1993.

[63] B. Claflin and H. Fritzsche, "The Role of Oxygen Diffusion in Photoinduced Changes of the Electronic and Optical Properties in Amorphous Indium oxide," *Journal of Electronic Materials,* vol. 25, p. 1772, 1996.

[64] E. Burstein, "Anomalous optical Absorption Limit in InSb," *Physical Review,* vol. 93, p. 632, 1954.

[65] R. Martins, P. Almeida, P. Barquinha, L. Pereira, A. Pimentel, I. Ferriera, and E. Fortunato, "Electron transport and optical characteristics in amorphous indium zinc oxide films," *Journal of Non-Crystalline Solids,* vol. 352, pp. 1471-1474, 2006.

[66] R. B. Iverson and R. Reif, "Temperature depenence of the crystallization parameter," *Journal of Applied Physics,* vol. 62, pp. 1675-1681, September 1, 1987.

[67] D. C. Paine, T. Whitson, D. Janiac, R. Beresford, and C. O. Yang, "A study of low temperature crystallization of amorphous thin film indium-tin-oxide," *Journal of Applied Physics,* vol. 85, pp. 8445-8450, June 15th, 1999.

[68] J. N. Lee, B. J. Lee, D. G. Moon, and B. T. Ahn, "Effect of Deposition Temperature on the Crystallization Mechanism of Amorphous Silicon Films on Glass," *Japan Journal of Applied Physics,* vol. 36, pp. 6862-6866, November 11, 1997.

APPENDIX – MATERIAL SAFETY DATA SHEETS

SIGMA-ALDRICH
MATERIAL SAFETY DATA SHEET

Section 1 - Product and Company Information

Product Name	INDIUM(III) OXIDE, SINTERED, PIECES,3-12MM, 99.99+%
Product Number	342998
Brand	ALDRICH
Company	Sigma-Aldrich
Street Address	3050 Spruce Street
City, State, Zip, Country	SAINT LOUIS MO 63103 US
Technical Phone:	314 771 5765
Emergency Phone:	414 273 3850 Ext. 5996
Fax:	800 325 5052

Section 2 - Composition/Information on Ingredient

Substance Name	CAS #	SARA 313
INDIUM(III) OXIDE	1312-43-2	No

Formula In2O3
Synonyms Diindium trioxide * India * Indium (III) oxide * Indium (3+) oxide * Indium sesquioxide * Indium trioxide
RTECS Number: NL1770000

Section 3 - Hazards Identification

EMERGENCY OVERVIEW

Irritant.

Irritating to eyes, respiratory system and skin.

HMIS RATING

HEALTH: 2
FLAMMABILITY: 0
REACTIVITY: 0

NFPA RATING

HEALTH: 2
FLAMMABILITY: 0
REACTIVITY: 0

For additional information on toxicity, please refer to Section 11.

Section 4 - First Aid Measures

ORAL EXPOSURE

If swallowed, wash out mouth with water provided person is conscious. Call a physician.

INHALATION EXPOSURE

If inhaled, remove to fresh air. If not breathing give artificial respiration. If breathing is difficult, give oxygen.

DERMAL EXPOSURE

In case of contact, immediately wash skin with soap and copious amounts of water.

EYE EXPOSURE

In case of contact, immediately flush eyes with copious amounts of water for at least 15 minutes.

Section 5 - Fire Fighting Measures

FLASH POINT

N/A

AUTOIGNITION TEMP

N/A

FLAMMABILITY

N/A

EXTINGUISHING MEDIA

Suitable: Water spray. Carbon dioxide, dry chemical powder, or appropriate foam.

FIREFIGHTING

Protective Equipment: Wear self-contained breathing apparatus and protective clothing to prevent contact with skin and eyes.

Specific Hazard(s): Emits toxic fumes under fire conditions.

Section 6 - Accidental Release Measures

PROCEDURE(S) OF PERSONAL PRECAUTION(S)

Wear respirator, chemical safety goggles, rubber boots, and heavy rubber gloves.

METHODS FOR CLEANING UP

Sweep up, place in a bag and hold for waste disposal. Avoid raising dust. Ventilate area and wash spill site after material pickup is complete.

Section 7 - Handling and Storage

HANDLING

User Exposure: Do not breathe dust. Avoid contact with eyes, skin, and clothing. Avoid prolonged or repeated exposure.

STORAGE

Suitable: Keep tightly closed.

Section 8 - Exposure Controls / PPE

ENGINEERING CONTROLS

Safety shower and eye bath. Mechanical exhaust required.

PERSONAL PROTECTIVE EQUIPMENT

Respiratory: Government approved respirator.

Hand: Compatible chemical-resistant gloves.

Eye: Chemical safety goggles.

GENERAL HYGIENE MEASURES

Wash thoroughly after handling.

Section 9 - Physical/Chemical Properties

Appearance	Physical State: Solid Color: Slightly yellow Form: Powder	

Property	Value	At Temperature or Pressure
Molecular Weight	277.64 AMU	
pH	N/A	
BP/BP Range	N/A	
MP/MP Range	N/A	
Freezing Point	N/A	
Vapor Pressure	< 0.01 mmHg	25 °C
Vapor Density	N/A	
Sat. Vapor Conc.	N/A	
SG/Density	7.179 g/cm3	
Bulk Density	N/A	

Odor Threshold	N/A
Volatile%	N/A
VOC Content	N/A
Water Content	N/A
Solvent Content	N/A
Evaporation Rate	N/A
Viscosity	N/A
Surface Tension	N/A
Partition Coef.	N/A
Decomposition Temp.	N/A
Flash Point	N/A
Explosion Limits	N/A
Flammability	N/A
Autoignition Temp	N/A
Refractive Index	N/A
Optical Rotation	N/A
Miscellaneous Data	N/A
Solubility	N/A

N/A = not available

Section 10 - Stability and Reactivity

STABILITY

Stable: Stable.

Materials to Avoid: Strong oxidizing agents.

HAZARDOUS DECOMPOSITION PRODUCTS

Hazardous Decomposition Products: Indium/indium oxides.

HAZARDOUS POLYMERIZATION

Hazardous Polymerization: Will not occur

Section 11 - Toxicological Information

ROUTE OF EXPOSURE

Skin Contact: Causes skin irritation.

Skin Absorption: May be harmful if absorbed through the skin.

Eye Contact: Causes eye irritation.

Inhalation: Material is irritating to mucous membranes and upper respiratory tract. May be harmful if inhaled.

Ingestion: May be harmful if swallowed.

SIGNS AND SYMPTOMS OF EXPOSURE

To the best of our knowledge, the chemical, physical, and toxicological properties have not been thoroughly investigated.

Section 12 - Ecological Information

Section 13 - Disposal Considerations

APPROPRIATE METHOD OF DISPOSAL OF SUBSTANCE OR PREPARATION

Contact a licensed professional waste disposal service to dispose of this material. Observe all federal, state, and local environmental regulations.

Section 14 - Transport Information

DOT

Proper Shipping Name: None

Non-Hazardous for Transport: This substance is considered to be non-hazardous for transport.

IATA

Non-Hazardous for Air Transport: Non-hazardous for air

transport.

Section 15 - Regulatory Information

EU ADDITIONAL CLASSIFICATION

Symbol of Danger: Xi

Indication of Danger: Irritant.

R: 36/37/38

Risk Statements: Irritating to eyes, respiratory system and skin.

S: 26 36

Safety Statements: In case of contact with eyes, rinse immediately with plenty of water and seek medical advice. Wear suitable protective clothing.

US CLASSIFICATION AND LABEL TEXT

Indication of Danger: Irritant.

Risk Statements: Irritating to eyes, respiratory system and skin.

Safety Statements: In case of contact with eyes, rinse immediately with plenty of water and seek medical advice. Wear suitable protective clothing.

UNITED STATES REGULATORY INFORMATION

SARA LISTED: No

TSCA INVENTORY ITEM: Yes

CANADA REGULATORY INFORMATION

WHMIS Classification: This product has been classified in accordance with the hazard criteria of the CPR, and the MSDS contains all the information required by the CPR.

DSL: Yes

NDSL: No

SIGMA-ALDRICH

MATERIAL SAFETY DATA SHEET

SECTION 1. - - - - - - - - - - CHEMICAL IDENTIFICATION- - - - - - - - - -

CATALOG #: 205532

NAME: ZINC OXIDE, POWDER, <1 MICRON, 99.9%

SECTION 2. - - - - - COMPOSITION/INFORMATION ON INGREDIENTS - - - - - -

CAS #: 1314-13-2

MF: OZN

EC NO: 215-222-5

SYNONYMS

ACTOX 14 * ACTOX 16 * ACTOX 216 * AI3-00277 * AKRO-ZINC BAR 85 * AKROZINC BAR 90 * AMALOX * AZO-33 * AZO-55 * AZO-66 * AZO-77 * AZODOX-55 * AZODOX-55TT * AZO-55TT * AZO-66TT * AZO-77TT * CADOX XX 78 * CHINESE WHITE * C.I. 77947 * C.I. PIGMENT WHITE 4 * CYNKU TLENEK (POLISH) * ELECTOX 2500 * EMANAY ZINC OXIDE * EMAR * FELLING ZINC OXIDE * FLOWERS OF ZINC * GIAP 10 * GREEN SEAL-8 * HUBBUCK'S WHITE * KADOX 15 * KADOX-25 * KADOX 72 * K-ZINC * OUTMINE * OZIDE * OZLO * PERMANENT WHITE * PHILOSOPHER'S WOOL * POWDER BASE 900 * PROTOX TYPE 166 * PROTOX TYPE 167 * PROTOX TYPE 168 * PROTOX TYPE 169 * PROTOX TYPE 267 * PROTOX TYPE 268 * RED SEAL 9 * SNOW WHITE * UNICHEM ZO * VANDEM VAC * VANDEM VOC * WHITE SEAL-7 * XX 78 * XX 203 * XX 601 * ZINCA 20 * ZINCITE * ZINCOID * ZINC OXIDE (ACGIH:OSHA) * ZINC OXIDE FUME (OSHA) * ZINC WHITE * ZN-0401 E 3/16'' * ZN 0701T *

SECTION 3. - - - - - - - - - - HAZARDS IDENTIFICATION - - - - - - - - -

LABEL PRECAUTIONARY STATEMENTS

HARMFUL
HARMFUL BY INHALATION.
CAUTION: AVOID CONTACT AND INHALATION.
KEEP CONTAINER TIGHTLY CLOSED AND IN WELL-VENTILATED PLACE.

SECTION 4. - - - - - - - - - - FIRST-AID MEASURES- - - - - - - - - - -
IF SWALLOWED, WASH OUT MOUTH WITH WATER PROVIDED PERSON IS CONSCIOUS.
CALL A PHYSICIAN.
IF INHALED, REMOVE TO FRESH AIR. IF NOT BREATHING GIVE ARTIFICIAL
RESPIRATION. IF BREATHING IS DIFFICULT, GIVE OXYGEN.
IN CASE OF SKIN CONTACT, FLUSH WITH COPIOUS AMOUNTS OF WATER
FOR AT LEAST 15 MINUTES. REMOVE CONTAMINATED CLOTHING AND SHOES.
CALL A PHYSICIAN.
IN CASE OF CONTACT WITH EYES, FLUSH WITH COPIOUS AMOUNTS OF WATER FOR
AT LEAST 15 MINUTES. ASSURE ADEQUATE FLUSHING BY SEPARATING THE
EYELIDS WITH FINGERS. CALL A PHYSICIAN.

SECTION 5. - - - - - - - - - FIRE FIGHTING MEASURES - - - - - - - - - -
EXTINGUISHING MEDIA
WATER SPRAY.
CARBON DIOXIDE, DRY CHEMICAL POWDER OR APPROPRIATE FOAM.
SPECIAL FIREFIGHTING PROCEDURES
WEAR SELF-CONTAINED BREATHING APPARATUS AND PROTECTIVE CLOTHING
TO PREVENT CONTACT WITH SKIN AND EYES.
UNUSUAL FIRE AND EXPLOSIONS HAZARDS
EMITS TOXIC FUMES UNDER FIRE CONDITIONS.

SECTION 6. - - - - - - - - ACCIDENTAL RELEASE MEASURES- - - - - - - - -
WEAR SELF-CONTAINED BREATHING APPARATUS, RUBBER BOOTS AND HEAVY
RUBBER GLOVES.
SWEEP UP, PLACE IN A BAG AND HOLD FOR WASTE DISPOSAL.
AVOID RAISING DUST.
VENTILATE AREA AND WASH SPILL SITE AFTER MATERIAL PICKUP IS COMPLETE.
EVACUATE AREA.

SECTION 7. - - - - - - - - - - HANDLING AND STORAGE- - - - - - - - - -
REFER TO SECTION 8.

SECTION 8. - - - - - - EXPOSURE CONTROLS/PERSONAL PROTECTION- - - - - -
SAFETY SHOWER AND EYE BATH.
MECHANICAL EXHAUST REQUIRED.
WASH THOROUGHLY AFTER HANDLING.
DO NOT BREATHE DUST.
AVOID CONTACT WITH EYES, SKIN AND CLOTHING.
AVOID PROLONGED OR REPEATED EXPOSURE.
NIOSH/MSHA-APPROVED RESPIRATOR.
COMPATIBLE CHEMICAL-RESISTANT GLOVES.
CHEMICAL SAFETY GOGGLES.
KEEP TIGHTLY CLOSED.
STORE IN A COOL DRY PLACE.

SECTION 9. - - - - - - - PHYSICAL AND CHEMICAL PROPERTIES - - - - - - -
APPEARANCE AND ODOR
WHITE POWDER
PHYSICAL PROPERTIES
SPECIFIC GRAVITY: 5.606
SWISS POISON CLASS: FREI

SECTION 10. - - - - - - - - -STABILITY AND REACTIVITY - - - - - - - - -

STABILITY

STABLE.

HAZARDOUS COMBUSTION OR DECOMPOSITION PRODUCTS

ZINC/ZINC OXIDES

HAZARDOUS POLYMERIZATION

WILL NOT OCCUR.

SECTION 11. - - - - - - - - - TOXICOLOGICAL INFORMATION - - - - - - - -

ACUTE EFFECTS

MAY CAUSE SKIN IRRITATION.
MAY BE HARMFUL IF ABSORBED THROUGH THE SKIN.
MAY CAUSE EYE IRRITATION.
HARMFUL IF INHALED.
MATERIAL MAY BE IRRITATING TO MUCOUS MEMBRANES AND UPPER RESPIRATORY TRACT.
MAY BE HARMFUL IF SWALLOWED.
ZINC OXIDE DUST OR FUME CAN IRRITATE THE RESPIRATORY TRACT.
PROLONGED SKIN CONTACT CAN PRODUCE A SEVERE DERMATITIS CALLED OXIDE POX.
EXPOSURE TO HIGH LEVELS OF DUST OR FUME CAN CAUSE METALLIC TASTE, MARKED THIRST, COUGHING, FATIGUE, WEAKNESS, MUSCULAR PAIN AND NAUSEA FOLLOWED BY FEVER AND CHILLS. SEVERE OVEREXPOSURE MAY RESULT IN BRONCHITIS OR PNEUMONIA WITH A BLUEISH TINT TO THE SKIN.

PROLONGED EXPOSURE CAN CAUSE:

REVERSIBLE LIVER ENZYME ABNORMALITIES.
DIARRHEA, PEPTIC ULCERATION AND GASTROINTESTINAL HEMORRHAGE MAY ALSO OCCUR.

RTECS #: ZH4810000

ZINC OXIDE

IRRITATION DATA

SKN-RBT 500 MG/24H MLD 28ZPAK -,10,1972
EYE-RBT 500 MG/24H MLD 28ZPAK -,10,1972

TOXICITY DATA

ORL-HMN LDLO:500 MG/KG YAKUD5 22,291,1980
IPR-RAT LD50:240 MG/KG ZDKAA8 38(9),18,1978
ORL-MUS LD50:7950 MG/KG GISAAA 51(4),89,1986
IHL-MUS LC50:2500 MG/M3 IPSTB3 3,93,1976

TARGET ORGAN DATA

LUNGS, THORAX OR RESPIRATION (OTHER CHANGES)
BIOCHEMICAL EFFECTS (DEHYDROGENASES)
BIOCHEMICAL EFFECTS (OTHER ENZYMES)
ONLY SELECTED REGISTRY OF TOXIC EFFECTS OF CHEMICAL SUBSTANCES (RTECS) DATA IS PRESENTED HERE. SEE ACTUAL ENTRY IN RTECS FOR COMPLETE INFORMATION.

SECTION 12. - - - - - - - - - ECOLOGICAL INFORMATION - - - - - - - - -

DATA NOT YET AVAILABLE.

SECTION 13. - - - - - - - - - DISPOSAL CONSIDERATIONS - - - - - - - - -

CONTACT A LICENSED PROFESSIONAL WASTE DISPOSAL SERVICE TO DISPOSE OF THIS MATERIAL.

OBSERVE ALL FEDERAL, STATE AND LOCAL ENVIRONMENTAL REGULATIONS.

SECTION 14. - - - - - - - - - - TRANSPORT INFORMATION - - - - - - - - -

CONTACT ALDRICH CHEMICAL COMPANY FOR TRANSPORTATION INFORMATION.

SECTION 15. - - - - - - - - - REGULATORY INFORMATION - - - - - - - - -

EUROPEAN INFORMATION

HARMFUL

R 20

HARMFUL BY INHALATION.

S 7/9

KEEP CONTAINER TIGHTLY CLOSED AND IN WELL-VENTILATED PLACE.

REVIEWS, STANDARDS, AND REGULATIONS

OEL=MAK

ACGIH TLV-STEL 10 MG/M3, FUME DTLVS* TLV/BEI,1997

ACGIH TLV-TWA 10 MG/M3 (DUST) DTLVS* TLV/BEI,1999

ACGIH TLV-TWA 5 MG/M3; STEL 10 MG/M3 (FUME) DTLVS* TLV/BEI,1999

EPA FIFRA 1988 PESTICIDE SUBJECT TO REGISTRATION OR RE-REGISTRATION FEREAC 54,7740,1989

MSHA STANDARD-AIR:TWA 5 MG/M3 (FUME)

DTLVS* 3,284,1971

OSHA PEL (GEN INDU):8H TWA 5 MG/M3, FUME AND RESPIRABLE FRACTION

CFRGBR 29,1910.1000,1994

OSHA PEL (GEN INDU):8H TWA 15 MG/M3, TOTAL DUST

CFRGBR 29,1910.1000,1994

OSHA PEL (CONSTRUC):8H TWA 5 MG/M3, FUME AND RESPIRABLE FRACTION

CFRGBR 29,1926.55,1994

OSHA PEL (CONSTRUC):8H TWA 15 MG/M3, TOTAL DUST

CFRGBR 29,1926.55,1994

OSHA PEL (SHIPYARD):8H TWA 5 MG/M3, FUME AND RESPIRABLE FRACTION

CFRGBR 29,1915.1000,1993

OSHA PEL (SHIPYARD):8H TWA 15 MG/M3, TOTAL DUST

CFRGBR 29,1915.1000,1993

OSHA PEL (FED CONT):8H TWA 5 MG/M3

CFRGBR 41,50-204.50,1994

OEL-ARAB REPUBLIC OF EGYPT: TWA 5 MG/M3, JAN1993

OEL-AUSTRALIA: TWA 10 MG/M3, JAN1993

OEL-AUSTRALIA: TWA 5 MG/M3, STEL 10 MG/M3 (FUME), JAN1993

OEL-BELGIUM: TWA 10 MG/M3, JAN1993

OEL-DENMARK: TWA 4 MG(ZN)/M3, JAN1999

OEL-BELGIUM: TWA 5 MG/M3, STEL 10 MG/M3 (FUME), JAN1993

OEL-FINLAND: TWA 5 MG/M3 (FUME), JAN1999

OEL-FRANCE: VME (DUST) 10 MG/M3, JAN1999

OEL-FRANCE: VME (FUME) 5 MG/M3, JAN1999

OEL-GERMANY: MAK 5 MG/M3 (FUME), JAN1999

OEL-HUNGARY: TWA 5 MG/M3, JAN1993

OEL-JAPAN: OEL 5 MG/M3 (FUME), JAN1999

OEL-THE NETHERLANDS: MAC-TGG 5 MG/M3, JAN1999

OEL-NORWAY: TWA 5 MG/M3, JAN1999

OEL-THE PHILIPPINES: TWA 1 MG/M3, JAN1993

OEL-POLAND: MAC(TWA) FUME 5 MG/M3, MAC(STEL) FUME 10 MG/M3, JAN1999

OEL-SWEDEN: NGV 5 MG/M3, JAN1999

OEL-SWITZERLAND: MAK-W 5 MG/M3, JAN1999

OEL-THAILAND: TWA 5 MG/M3 (FUME), JAN1993

OEL-TURKEY: TWA 5 MG/M3, JAN1993

OEL-UNITED KINGDOM: TWA 5 MG/M3, STEL 10 MG/M3, FUME, SEP2000

OEL IN ARGENTINA, BULGARIA, COLOMBIA, JORDAN, KOREA CHECK ACGIH TLV;

OEL IN NEW ZEALAND, SINGAPORE, VIETNAM CHECK ACGIH TLV

NIOSH REL TO ZINC OXIDE, FUME-AIR:10H TWA 5 MG/M3;STEL 10 MG/M3

NIOSH* DHHS #92-100,1992

NIOSH REL TO ZINC OXIDE, TOTAL DUST-AIR:TWA 5 MG/M3;CL 15

MG/M3/15M
NIOSH* DHHS #92-100,1992
NOES 1983: HZD X5686; NIS 295; TNF 56635; NOS 168; TNE 919197; TFE
151582
NOES 1983: HZD X9509; NIS 1; TNF 7; NOS 1; TNE 105; TFE 7
EPA TSCA SECTION 8(B) CHEMICAL INVENTORY
EPA TSCA SECTION 8(D) UNPUBLISHED HEALTH/SAFETY STUDIES
EPA TSCA TEST SUBMISSION (TSCATS) DATA BASE, JANUARY 2001
NIOSH ANALYTICAL METHOD, 1994: ELEMENTS BY ICP, 7300
NIOSH ANALYTICAL METHOD, 1994: ZINC AND COMPOUNDS, 7030 OR 7502
OSHA ANALYTICAL METHOD #ID-143
OSHA ANALYTICAL METHOD #ID-125G
U.S. INFORMATION
THIS PRODUCT IS SUBJECT TO SARA SECTION 313 REPORTING REQUIREMENTS.

SECTION 16. - - - - - - - - - - - OTHER INFORMATION- - - - - - - - - - -